

# Fast jets from bubbles close to solid objects: examples from pillars in water to infinite planes in different liquids

Christiane Lechner<sup>1\*</sup>, Max Koch<sup>2</sup>, Werner Lauterborn<sup>2</sup>, and Robert Mettin<sup>2</sup>

<sup>1</sup> TU Wien, Institute of Fluid Mechanics and Heat Transfer, Getreidemarkt 9, 1060 Vienna, Austria

<sup>2</sup> Georg-August-University Göttingen, Third Institute of Physics, Friedrich-Hund-Platz 1, 37077 Göttingen, Germany

## Abstract:

The dynamics of a single, laser-induced cavitation bubble on top of a solid cylinder and right at a plane solid boundary is studied both experimentally and numerically. The most intriguing phenomenon that occurs for a millimeter sized bubble *right at a flat solid boundary* in water is the formation of a fast jet that is directed towards the solid with a speed of the order of 1000 m/s. Paradoxically, in this setting, fast jet formation causally is related to the viscosity of the liquid. Thus, results from numerical simulations with varying liquid viscosity and bubble size are presented. Bubble dynamics and jet formation mechanisms are discussed. It is shown, that fast jet formation persists for a wide range of liquid viscosities, including e.g. 50 cSt silicone oil. For bubbles generated *close to the flat top of a long, thin cylinder* the parameter space of initial distance to the cylinder, bubble size and cylinder radius is scanned numerically and partly compared to experiments. When the maximum radius of the bubble exceeds the one of the cylinder the bubble collapses in the form of a mushroom or can resemble a trophy, depending on the values of the geometry parameters. Complex patterns of jet formation with jet speeds ranging from the order of a few hundred m/s to several thousand m/s are found. The results represent a contribution to understand the behavior of bubbles collapsing close to solid surfaces, in particular, how thin, fast jets are generated.

**Keywords:** bubble dynamics, cavitation, erosion, finite volume method, high-speed imaging, jet formation

## 1 Introduction

Due to their erosive power, cavitation bubbles collapsing close to solid boundaries have been subject to intense investigations for several decades. Mainly two phenomena associated with the collapse of the bubble are considered responsible for the destructive action: a high-speed, axial liquid jet directed towards the solid, and the shock waves emitted after the collapse of the resulting torus bubble.

Usually, jets form by involution of the bubble interface and reach a speed of the order of 100 m/s under normal ambient conditions (Philipp and Lauterborn (1998); Brujan et al. (2001); Supponen et al. (2016); Lechner et al. (2020)). A diagram comparing these data of jet velocities in dependence on the normalized distance of a bubble from a plane solid boundary,  $D^*$ , can be found in (Koch et al., 2022, Fig. 21).  $D^*$  is defined there as  $D^* = D_{\text{init}}/R_{\text{max}}$ , where  $D_{\text{init}}$  is the distance of the bubble center from the boundary and  $R_{\text{max}}$  is the radius of the bubble it would attain in a free liquid. For bubbles expanding and collapsing in ultimate proximity to the solid, however, very thin axial jets of the order of 1000 m/s are formed, following the violent self-impact of annular liquid inflow at the axis of symmetry (Lechner et al. (2019); Pishchalnikov et al. (2019); Lechner et al. (2020); Koch (2020); Koch et al. (2021) and Reuter and Ohl (2021)).

First photographs of this type of fast jet have been given in Benjamin and Ellis (1966) for a bubble under reduced ambient pressure, however, no interpretation could be given then. Photographic evidence of the fast jet under normal ambient conditions could only be given recently in (Koch, 2020; Koch et al., 2021). With a combination of experimental photographs and ray-tracing a 3D numerical simulation a lower bound of 732 m/s was estimated for the speed of the fast jet. Shortly thereafter, Reuter and Ohl (2021) presented new experimental evidence for the fast jet, including photographic recordings of the shock wave that is emitted after self-impact of the annular inflow. A lower bound of 850 m/s for the average jet speed could be inferred from these photographs. Having found this different kind of jetting phenomenon, unknown till then, the question arose whether there are other boundary geometries that provoke it, as well. In the past, investigation of bubble dynamics near structured objects got less attention than studies on flat or smooth surfaces. However, it is known that cavitation bubbles can reach, clean and also damage crevices, holes, trenches and other complicated surface features (see, e.g., Kauer et al. (2018)). Up to now, owing to the large variety of structures and constraints, only a few cases were already investigated for single bubble dynamics. Among the solid boundaries and objects, there are a small hole (Karri et al., 2011), blind holes/crevices (Trummler et al., 2020), rectangular channels (Andrews et al., 2020), convex surfaces (Tomita et al., 2002), a thin gap (parallel plates) (Hsiao et al., 2013; Quah et al., 2018; Gonzalez-Avila et al., 2020), rigid spheres Li et al. (2019); Zevnik and Dular (2020), a pencil-like electrode and cylinders (Palanker et al., 2003; Koch et al., 2022; Kadivar et al., 2021b), ridges and grooves (Kim and Kim, 2020), a micro structured riblet (Kadivar et al., 2021a),

\* E-mail address: [christiane.lechner@tuwien.ac.at](mailto:christiane.lechner@tuwien.ac.at)

doi: [10.24352/UB.OVGU-2023-042](https://doi.org/10.24352/UB.OVGU-2023-042)

2023 | All rights reserved.

edges (Lauterborn, 1971; Zhang et al., 2020; Senegačnik et al., 2021) and corners (Brujan et al., 2018; Wang et al., 2020). Bubble dynamics on a plane top of a cylinder has been studied quite thoroughly by Koch et al. (2022). Fast jets occur again abundantly in extended parameter ranges, in particular farther away from the solid boundary as with an infinite plane solid. Such studies are important for cleaning of structured surfaces in microdevices (Okorn-Schmidt et al., 2014; Reuter and Mettin, 2016; Yamashita and Ando, 2019).

The dynamics of the bubbles, in particular the process of jet formation, is influenced by many factors, including, e.g., the properties of the liquid or the geometry of nearby objects. From the wealth of possible geometrical configurations we concentrate on bubbles *right at a flat solid boundary* and on bubbles *close to the top of a rigid cylinder*. For bubbles expanding and collapsing right at a flat solid boundary, liquid viscosity has been identified to be decisive for the formation of the fast jet (see Lechner et al. (2019, 2020)). It is therefore of interest to quantify the influence of viscosity and bubble size on the jet formation process. Bubbles expanding and collapsing right at a solid boundary in liquids with different viscosities have been investigated experimentally by Gonzalez Avila et al. (2015) and Hupfeld et al. (2020) in different contexts. Gonzalez Avila et al. (2015) generated millimeter sized bubbles by electric sparks at a flat plate, which had a hole. The liquid viscosity was increased by using various silicone oils up to 100 cSt. The bubble evolution was monitored. The main interest was the ejection of liquid through the hole after bubble generation and after the first collapse. Hupfeld et al. (2020) experimentally investigated bubble dynamics at a flat solid surface in highly viscous liquids in the context of laser-ablation in liquids. Bubble shapes deviating strongly from hemi-spherical shape during the collapse phase were recorded with high-speed imaging. The interlayer, that forms between bubble and solid during the expansion phase, was investigated in detail. Jet formation was not investigated in these works. Numerically, the influence of viscosity and bubble size on bubble dynamics was investigated, e.g., in Reuter et al. (2022b) for bubbles close to a flat solid surface and in Saini et al. (2022) for bubbles with a pre-defined shape at maximum extension. Bubbles close to the top of a rigid cylinder, with the bubble exceeding the edge of the cylinder during maximum extension, have been studied in Koch et al. (2022) for a range of geometric parameters. For the major part of cases the bubbles collapse in the form of a mushroom and fast jets are generated from liquid self-impact at the axis of symmetry. For certain parameter configurations, however, the jet formation process is more involved. More than one self-impact event at the axis can occur, leading to a sequence of fast jets. Examples for this phenomenon are described here.

The numerical investigation of the dynamics of a bubble close to a flat, solid boundary for varying liquid viscosity and bubble size is described in this manuscript, as well as the dynamics of a bubble close to the top of a rigid cylinder with both experimental and numerical approaches. A standard method to generate single cavitation bubbles experimentally is via focusing a short, high intensity laser pulse into a cuvette filled with the liquid in question, mostly water. In the focal spot a short-living plasma is formed, due to optical breakdown. From that high-pressure spot, a cavitation bubble expands with emission of a shockwave. Due to the ambient pressure it will collapse again violently and emit further shockwaves.

The bubble *close to a cylinder* is generated on the symmetry axis of the cylinder. Therefore, three independent parameters describe the geometrical arrangement as shown in Figure 1:  $l_p$  — the length of the cylinder (height above a planar, solid boundary),  $r_p$  — the radius of the cylinder and  $D_{\text{init}}$  — the distance of the bubble to the top of the cylinder at  $t = 0$  (i.e. the spot of optical breakdown, hence the plasma spot). The energy of the bubble, given a certain atmospheric pressure, is classified by the maximum radius  $R_{\text{max}}^{\infty}$  — denoted by  $R_{\text{max}}$  for short in other works, and by  $R_{\text{max,unbound}}$  in Koch (2020); Koch et al. (2021, 2022) — the bubble would attain in an unbounded liquid. When the bubble is generated close to an object, the maximum, volume-equivalent radius  $R_{\text{max}}^{\text{eq}}$  will differ from the unbounded one, depending on the structure of the object and  $D_{\text{init}}$  (see also Lauterborn et al. (2018) and (Koch, 2020, Fig. 6.12)). The case of a long, thin cylinder,  $l_p \gg r_p$  and  $r_p < R_{\text{max}}^{\infty}$ , is considered here.

A bubble *right at a flat solid boundary* can be viewed as a special case of a bubble close to a cylinder with parameters  $r_p \rightarrow \infty$  and  $D_{\text{init}} = 0$ , see Fig. 1 (right). In low viscosity liquids the bubble expands to an approximately hemi-spherical shape. Thus, the equivalent radius of a hemi-sphere,

$$\mathcal{R}_{\text{max}}^{\text{eq}} := (3V_{\text{max}} / (2\pi))^{1/3}, \quad (1)$$

with  $V_{\text{max}}$  the maximum volume of the bubble, is a good measure of bubble size in this case.

This work is organized as follows: we present the bubble model and the numerical implementation in Section 2. Experimental methods for investigating bubbles close to a cylinder are briefly described in Sec. 3. The setup and parameter variations are specified in Sec. 4. Results from the parameter studies are presented in Section 5 and conclusions are given in Section 6.

## 2 Bubble Model and Numerical Implementation

The bubble model consists of a bubble filled with a small amount of non-condensable gas (air) surrounded by a liquid. The gas is taken to be ideal, undergoing adiabatic changes of state,  $p\rho_g^{-\gamma_g} = \text{const}$ , with  $p$  the pressure,  $\rho_g$  the density of the gas and  $\gamma_g$  the ratio of specific heats ( $\gamma_g = 1.4$  for air). Phase transition is not considered here. The liquid is modeled as a compressible fluid with the Tait equation of state,  $(p + B)\rho_l^{-n_T} = \text{const}$ , with  $\rho_l$  the density of the liquid,  $B$  the Tait pressure and  $n_T$  the Tait exponent, taken to be  $B = 305$  MPa,  $n_T = 7.15$  here. The vapor pressure is small compared to the ambient pressure of  $p_{\infty} = 101315$  Pa and therefore is neglected. Thermodynamic effects, mass exchange through the bubble wall as well as gravity are neglected. Liquid and gas are considered as viscous fluids. In particular, including the viscosity of the liquid is essential for fast jet formation for bubbles at a plane solid boundary. Surface tension is included for the bubbles at the flat solid boundary, but it is not essential for the findings presented here.

The equations are formulated for a single fluid with density  $\rho$ , pressure  $p$  and velocity  $\mathbf{u}$  satisfying the Navier-Stokes equation (2) and continuity equation (3). In order to distinguish between the two phases liquid and gas, volume fractions  $\alpha_l$  and  $\alpha_g$  are introduced, with  $\alpha_l = 1$  in the liquid phase and  $\alpha_l = 0$  in the gas phase and  $\alpha_g = 1 - \alpha_l$ . Since no mass transfer across the interface is considered, the individual phases satisfy the continuity equations (4).

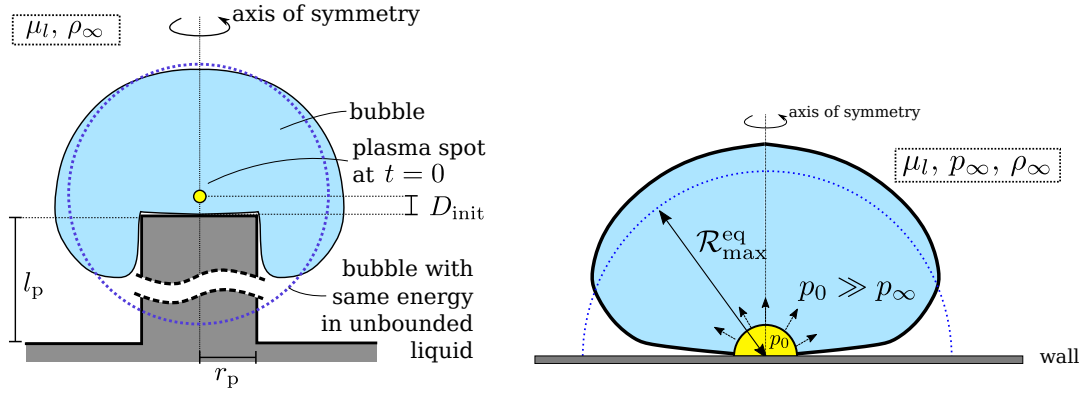


Fig. 1: Sketch of the parameters for classification of bubbles close to a solid cylinder ( $l_p \gg r_p$ ) and close to a flat, solid boundary ( $r_p \rightarrow \infty$ ) with varying liquids (parameters at equilibrium: density  $\rho_\infty$  and viscosity  $\mu_l$ ). Left: Sketch for a bubble on a pillar with a bubble larger than the pillar diameter. Figure taken from Koch et al. (2022) under licence CC BY 4.0, slightly modified. Right: Sketch of the numerical setup for the special case  $r_p \rightarrow \infty$ ,  $D_{\text{init}} = 0$ : A small hemi-spherical bubble with internal pressure  $p_0$  initially is placed directly at a solid boundary ("wall"). The bubble expands to some maximum volume. The radius of the volume equivalent hemi-sphere is denoted by  $\mathcal{R}_{\text{max}}^{\text{eq}}$ .

$$\frac{\partial(\rho \mathbf{u})}{\partial t} + \nabla \cdot (\rho \mathbf{u} \otimes \mathbf{u}) = -\nabla p + \nabla \cdot \mathbf{T} + \mathbf{f}_\sigma, \quad (2)$$

$$\frac{\partial \rho}{\partial t} + \nabla \cdot (\rho \mathbf{u}) = 0, \quad (3)$$

$$\frac{\partial(\alpha_i \rho_i)}{\partial t} + \nabla \cdot (\alpha_i \rho_i \mathbf{u}) = 0, \quad i = l, g. \quad (4)$$

$\nabla$  denotes the gradient,  $\nabla \cdot$  is the divergence, and  $\otimes$  the tensorial product. The density field,  $\rho$ , is written as  $\rho = \alpha_l \rho_l + \alpha_g \rho_g$ .  $\mathbf{T}$  is the viscous stress tensor of a Newtonian fluid,

$$\mathbf{T} = \mu \left( \nabla \mathbf{u} + (\nabla \mathbf{u})^T - \frac{2}{3} (\nabla \cdot \mathbf{u}) \mathbf{I} \right), \quad (5)$$

with  $\mu = \alpha_l \mu_l + \alpha_g \mu_g$ , where  $\mu_l, \mu_g$  are the dynamic viscosities of liquid and gas, taken to be constant here. Surface tension is included via a force density field  $\mathbf{f}_\sigma(\mathbf{x}, t)$  (see, e.g., Tryggvason et al., 2001).

Equations (2)–(4) are discretized with the finite volume method. The numerical implementation is based on the open source software package OpenFOAM (Weller et al., 1998) in the foam-extend fork (Gschaider et al., 2017). A pressure based two-phase solver is adapted for our purpose (see Koch et al., 2016).

Initially, a small bubble with high internal pressure  $p_0 \gg p_\infty$  is placed in the still liquid close to or directly at the solid surface. For bubble placed directly at the solid surface the initial shape is a hemi-sphere with radius  $\mathcal{R}_{\text{init}}$ . Bubbles placed at some distance  $D_{\text{init}}$  away from the solid initially have spherical shape with radius  $R_{\text{init}}$ .

At the solid surface no-slip boundary conditions are imposed for the velocity,  $\mathbf{u} = 0$ , the normal derivative of pressure is set to zero,  $\partial_n p = 0$ , and the liquid volume fraction  $\alpha_l$  is set to 1 at the solid. At the outer boundary approximate non-reflecting boundary conditions are specified for velocity and pressure.

Information on the computational grid and the time step is given in Secs 4.1 and 4.2.

### 3 Experimental Methods

The experimental method of the laser-induced bubble close to the top of the rigid cylinder is described briefly here. For a detailed explanation, the reader is referred to Koch et al. (2022). A sketch of the setup is given in Fig. 2.

The bubble is produced in the center of a rectangular cuvette of edge length 1 cm  $\times$  5 cm  $\times$  4 cm (width, depth, height), filled with de-ionized water. The laser for bubble seeding is an Nd:YAG Litron nano PIV, operated at  $\lambda = 532$  nm with a single pulse duration of 10 ns. The laser light is first widened and then focused into the center of the cuvette by a lens of 35 mm focal distance.

For the rigid cylinder, a sewing needle was ground to flat top. The needle radius was measured to be  $r_p = 272.8 \mu\text{m}$ .

Two cameras are applied for observing the bubble, each equipped with a long distance microscope objective (K2 Infinity). For Mega-frames per second recording of the collapse of the bubble the Imacon 468 was used (8 images in total) and for kilo-frames per second recording of the overall dynamics the Photron APS-RX was used. The trigger to start the recording of the Imacon camera has to be known with 1  $\mu\text{s}$  precision. This was accomplished with a continuous wave Helium-Neon laser that points onto a photodiode through the site of bubble generation. Backlight illumination was done with a xenon-flash (Mecablitz).

### 4 Setup and parameter variations

In the following, we describe the setup of the numerical investigations. Dimensionless parameters are defined as appropriate for the particular case. The parameter ranges that are investigated are specified.

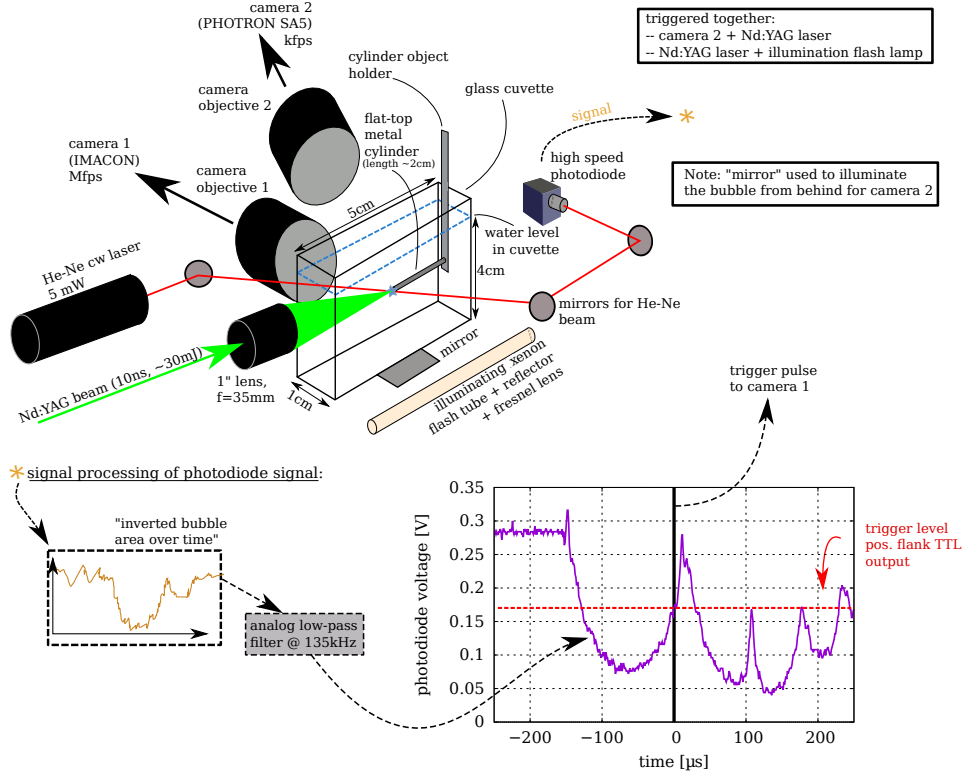


Fig. 2: Sketch of the experimental setup and trigger scheme to record the mushroom-shaped bubbles with two high-speed cameras. Figure taken from Koch et al. (2022) under licence CC BY 4.0.

#### 4.1 Numerical setup for bubbles directly at a flat solid boundary

Simulations are performed in axial symmetry, with the exception of the 3D simulation shown in Fig. 4, below. A sketch of the computational domain and the grid structure is given in Fig. 3. The center of the mesh is Cartesian ( $c$ ) with uniform grid spacing,  $\Delta x_{\min}$ , for  $|x|, y \leq r_1$ . Further out, a polar cell ordering ( $p$ ) is used with the grid spacing increasing progressively in radial direction. For  $r_2 < |x|, y < r_3$  the progression factor is such that the grid cells have aspect ratio 1. For  $r_3 < |x|, y$ , the progression factor is increased to 1.09. Typically, the grids consist of 120 000 to 200 000 cells for these series of runs. During the major part of bubble evolution the time step is adjusted such that the Courant number of the flow does not exceed 0.2 and the interface Courant number is less than 0.08. During the stages, where the compressibility of the liquid is important, the acoustic Courant number is well below 1. For bubbles expanding right at a plane solid boundary, the radius of the hemi-sphere,  $\mathcal{R}_{\max}^{\text{eq}}$ , that has the same volume as the bubble at maximum extension is taken as a length scale, see Eq. (1). A natural scale for velocity is the average collapse speed of a Rayleigh bubble in an inviscid liquid,  $\sqrt{p_{\infty}/\rho_{\infty}}$ , where  $p_{\infty}$  is the ambient pressure and  $\rho_{\infty}$  denotes the density of the liquid at ambient conditions. For the bubbles considered here,  $\mathcal{R}_{\max}^{\text{eq}}$  is of the order of 1 mm. For water and  $p_{\infty} = 1\text{bar}$  the characteristic velocity is 10 m/s. The influence of surface tension is small and can be neglected in the following considerations. The maximum bubble radius  $\mathcal{R}_{\max}^{\text{eq}}$ , the velocity scale  $\sqrt{p_{\infty}/\rho_{\infty}}$ , and the kinematic viscosity of the liquid,  $\nu_l = \mu_l/\rho_{\infty}$ , can be combined to yield a dimensionless number. In order to keep a direct relation with the viscosity of the liquid we define

$$\frac{1}{\text{Re}_b} = \frac{\nu_l}{\mathcal{R}_{\max}^{\text{eq}}} \sqrt{\frac{\rho_{\infty}}{p_{\infty}}}, \quad (6)$$

which corresponds to the inverse of a bubble Reynolds number  $\text{Re}_b$ .

Bubble dynamics is investigated by means of several series of simulations. Essentially, two parameters are varied, the bubble size and the viscosity of the liquid. A bubble that expands to  $\mathcal{R}_{\max}^{\text{eq}} = 627 \mu\text{m}$  under normal ambient conditions in water serves as reference for the parameter study. The corresponding inverse Reynolds number for this reference bubble evaluates to  $1/\text{Re}_b = 1.59 \times 10^{-4}$ .

Four one-parameter series of simulations are presented.

- In **series 1** the liquid viscosity is varied between  $\mu_l = 0.125\mu_{H_2O}$  and  $\mu_l = 300\mu_{H_2O}$ , while initial data  $\mathcal{R}_{\text{init}} = 2^{1/3}20 \mu\text{m}$ ,  $p_0 = 1.1 \times 10^4 \text{bar}$  are kept fixed. The reference bubble is included in this series. A computational grid with  $\Delta x_{\min} = 1 \mu\text{m}$ ,  $r_1 = 150 \mu\text{m}$  and  $r_3 \geq 1.1\mathcal{R}_{\max}^{\text{eq}}$  is chosen for this series. The outer boundary is located at  $r_4 \approx 0.25\text{m}$ . For the liquid with the highest viscosity leading to an inverse bubble Reynolds number of  $1/\text{Re}_b = 6.25 \times 10^{-2}$  an additional restriction on the maximum value of the time step is necessary to prevent instabilities of the bubble interface.

The inverse bubble Reynolds numbers for the bubbles in series 1 lie in the interval  $1/\text{Re}_b \in [2 \times 10^{-5}, 6.25 \times 10^{-2}]$ .

- For **series 2–4** the liquid properties are kept fixed and the maximum radius of the bubble is varied by changing initial data. In order to achieve this, starting from the initial data of series 1, all lengths, as e.g. the initial radius  $\mathcal{R}_{\text{init}}$  are scaled by a

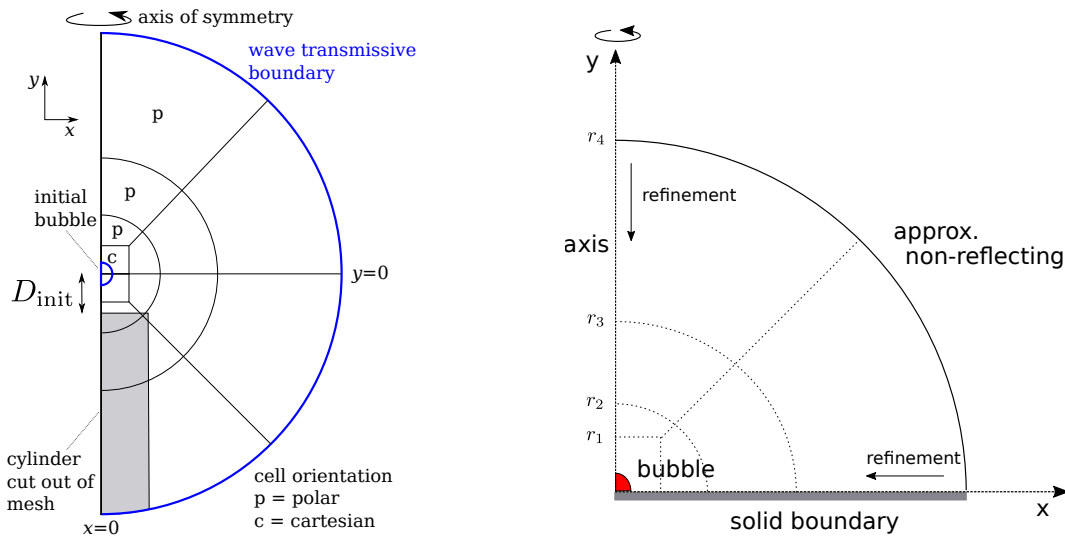


Fig. 3: Sketch of the computational domain and the grid structure (not to scale). Left: for the bubbles close to the top of a rigid cylinder. Figure taken from Koch et al. (2022) under licence CC BY 4.0. Right: for the bubbles close to a flat, solid boundary. Figure adapted with permission from Lechner et al. (2020). Copyrighted by the American Physical Society.

factor ranging from 0.5 to 8, while the initial pressure in the bubble is kept constant. The computational grid is scaled by the same factor. Accordingly, e.g. the minimum grid spacing in the Cartesian inner region ranges from  $\Delta x_{\min} = 0.5 \mu\text{m}$  to  $8 \mu\text{m}$ . This strategy is adopted to keep the total amount of cells and thereby the computational effort reasonably small for the parameter study. Grid independence is discussed in Appendix A.1.

The three liquids under consideration in series 2–4 are water and 30 cSt and 50 cSt silicone oils. Material properties of the 30 cSt silicone oil are  $\rho_{\infty} = 971 \text{ kg/m}^3$ ,  $\mu_1 = 0.029 \text{ kg/(ms)}$  yielding  $\nu_1 = 29.9 \times 10^{-6} \text{ m}^2/\text{s}$  and of the 50 cSt silicone oil  $\rho_{\infty} = 956 \text{ kg/m}^3$ ,  $\mu_1 = 0.0478 \text{ kg/(ms)}$ ,  $\nu_1 = 50 \times 10^{-6} \text{ m}^2/\text{s}$ . For water,  $\rho_{\infty} = 998.2 \text{ kg/m}^3$ ,  $\mu_1 = 0.001 \text{ kg/(ms)}$ , and  $\nu_1 = 1.0 \times 10^{-6} \text{ m}^2/\text{s}$ . The reference bubble is included in series 2. Overall, the maximum radii  $R_{\max}^{\text{eq}}$  vary between  $255 \mu\text{m}$  and  $5200 \mu\text{m}$ . The inverse bubble Reynolds numbers in series 2–4 span the range between  $2 \times 10^{-5}$  and  $1.9 \times 10^{-2}$ .

## 4.2 Setup for bubbles close to the top of a cylinder

For the investigation on bubbles close to the top of a rigid cylinder, the liquid is taken to be water ( $\rho_{\infty} = 998.2 \text{ kg/m}^3$ ) and the geometry parameters are varied. The calculations were done with setting the surface tension to zero. This does not affect the solution as stated in Lechner et al. (2020); Koch (2020). The maximum radius,  $R_{\max}^{\infty}$ , the bubble would attain in a free liquid, is introduced as a length scale. Three other lengths enter the scenario: the length  $l_p$  of the cylinder, the radius  $r_p$  of the cylinder and the initial distance,  $D_{\text{init}}$ , of the bubble from the top of the cylinder, see Fig. 1. The cylinder is assumed to be long,  $l_p \gg r_p$ , and slim when compared to the bubble size,  $r_p < R_{\max}$ , such that the limit  $l_p \rightarrow \infty$  can be considered. Then, only three lengths  $r_p$ ,  $D_{\text{init}}$  and  $R_{\max}^{\infty}$  have to be specified. From these the two dimensionless parameters

$$D^* := \frac{D_{\text{init}}}{R_{\max}^{\infty}}, \quad r_p^* := \frac{r_p}{R_{\max}^{\infty}}, \quad (7)$$

are formed. In the following, cases with  $r_p^* \in [0.251, 0.893]$  and  $D^* \in [0.047, 2.009]$  are considered.

The simulations presented here for the bubbles close to the top of a rigid cylinder are performed in axial symmetry. For comparison to simulations in full 3D, the reader is referred to the original work (Koch et al. (2022)). A sketch of the computational domain and the grid structure of the present work is given in Fig. 3, left frame. The size of the computational domain was chosen to be  $52 \text{ mm}$ , while the maximum radii  $R_{\max}^{\infty}$  of the bubbles ranged from  $224 \mu\text{m}$  to  $636 \mu\text{m}$ . The cells in the center of the mesh (the region from  $x, y = 0$  to  $r_1 = 80 \mu\text{m}$ , compare right frame in Fig. 1) are oriented in a Cartesian way (c) with a uniform cell edge length of  $\Delta x = 1 \mu\text{m}$ . The region from  $r_1$  to  $r_2$ , next to the Cartesian one, is meant to adapt from Cartesian to polar orientation (p). The subsequent region with cells of polar orientation ranges up to  $r_3 \approx R_{\max}^{\infty}$ . Each cell has an approximate edge length ratio of 1 until this distance. Further out, the cell edge length in radial direction is increased progressively. There are no hanging nodes nor sudden resolution changes in the mesh. The cylinder with a radius of either  $200 \mu\text{m}$  or  $160 \mu\text{m}$  was cut out of the mesh.

At  $t = 0$  the liquid is at rest and the bubble is compressed to  $20 \mu\text{m}$  in all of the cases studied. The boundary condition at the cylinder is set to no-slip and  $\alpha = 1$  (= liquid). The outer boundary of the mesh is set to be wave transmissive.

The simulations in axial symmetry were done on a dual Xenon Silver 4216 machine with 32 cores and 93.1 GB RAM. Each simulation comprised about 125 000 cells and 30 000 time steps, consuming about 1h15min of computational time for  $110 \mu\text{s}$ .

## 5 Results

In the following, we describe the mechanism that leads to the formation of fast jets from bubbles expanding and collapsing right at a plane solid boundary in Sec. 5.1. Numerical results from varying the viscosity of the liquid and the bubble size are presented in Sec. 5.2. Experimental and numerical results for bubbles close to the top of a rigid cylinder are described in Secs. 5.3 and 5.4.

### 5.1 Millimeter sized bubble right at a flat solid boundary – mechanism of fast jet formation

Figure 5 gives an overview of the dynamics of a bubble with  $R_{\max}^{\text{eq}} = 627 \mu\text{m}$  expanding and collapsing right at the solid in water. The evolution shown in this figure ranges from the initial time,  $t = 0$ , where the bubble is generated, up to the first collapse. The figure shows results from a numerical simulation in axial symmetry. The collapse phase of a similar bubble also is shown in Fig. 4, which compares experimental high-speed photographs (top row) to the result of ray-tracing a numerical 3D simulation (bottom row), see Koch et al. (2021).

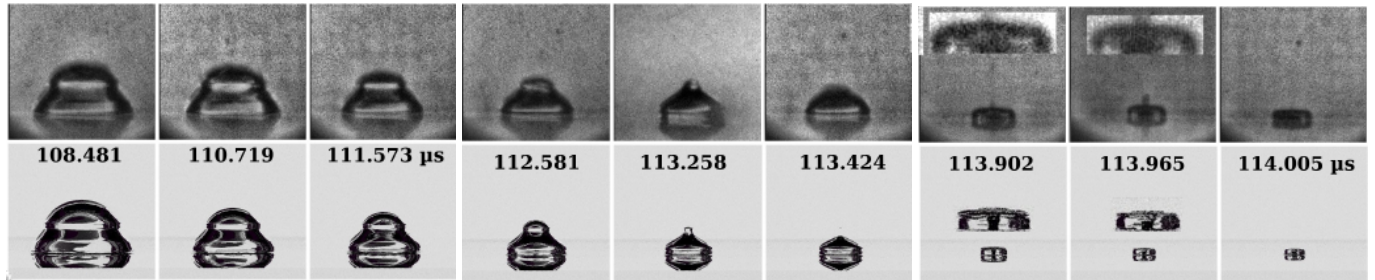


Fig. 4: Bubble collapsing right at a plane solid boundary in water. Figure taken from (Koch et al., 2021, part of Fig. 16) under licence CC BY 4.0, slightly modified. Comparison of experimental high-speed photographs (first row) and the result of ray-tracing a numerical 3D simulation (second row). In frames 7 and 8 of each row magnifications with enhanced contrast are shown as inserts. Frame width  $664.5 \mu\text{m}$ .

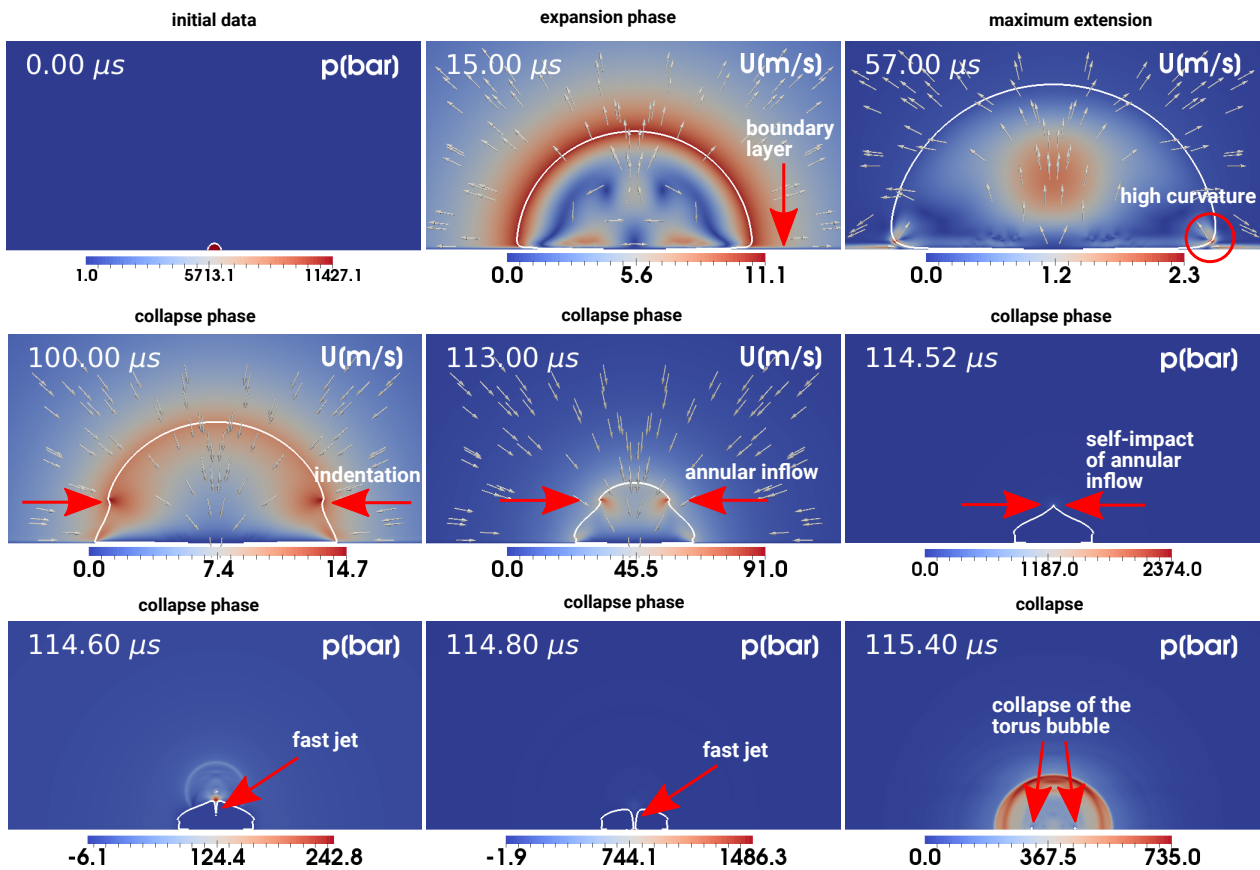


Fig. 5: Bubble expanding and collapsing right at a plane solid boundary in water. Results of an axially symmetric simulation. Shown is a cut through the bubble. The color gives the pressure in bar or the magnitude of the velocity in m/s, as indicated in the upper right corner of each frame. Small white arrows indicate the direction of the flow. The red arrows point at important steps in the dynamics of the bubble. At  $t = 57 \mu\text{s}$  the bubble attains the maximum volume with  $R_{\max}^{\text{eq}} = 627 \mu\text{m}$ . Frame size  $1.6 \text{ mm} \times 0.8 \text{ mm}$ .

Figure 5 shows the bubble shape together with the velocity or pressure field at several stages of bubble evolution. During the rapid expansion of the bubble a boundary layer adjacent to the solid forms, as indicated in frame 2 ( $t = 15 \mu\text{s}$ ). This boundary layer causes the outer rim of the bubble to slightly “lift-off” from the solid surface. At maximum extension the bubble shape is hemi-spherical, except for the region around the outer bubble rim, which exhibits a much larger curvature than the remainder of the bubble (frame 3,  $t = 57 \mu\text{s}$ ). For bubbles in a low viscosity liquid, such as water, this deviation from hemi-spherical shape might seem marginal. Nevertheless, it is decisive for the fast jet forming in the late collapse phase. The high curvature region at the outer rim collapses faster than the remainder of the bubble leading to an indentation, as shown in Figs 4 and 5 (frame 4 and 5,  $t = 100 \mu\text{s}$

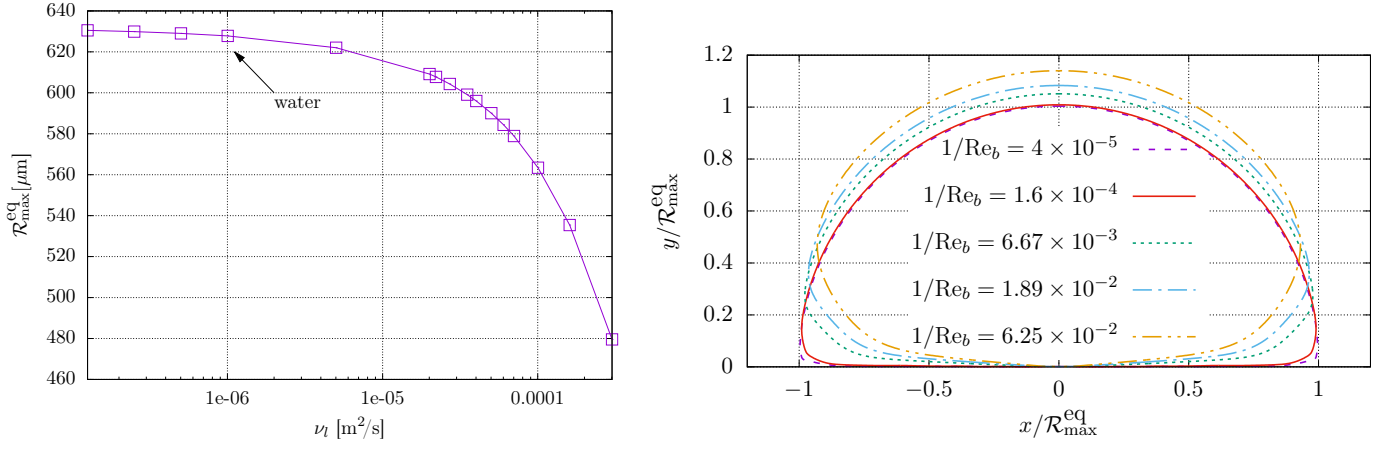


Fig. 6: Bubbles right at a flat solid boundary. Left: Maximum radius of the bubble as a function of  $\nu_l$  for series 1. The reference bubble is indicated by an arrow. Right: Bubble shapes at maximum extension for different values of  $1/\text{Re}_b$  taken from series 1,2 and 4. The solid line represents the reference bubble (water,  $\mathcal{R}_{\max}^{\text{eq}} = 627 \mu\text{m}$ ,  $1/\text{Re}_b = 1.59 \times 10^{-4}$ ).

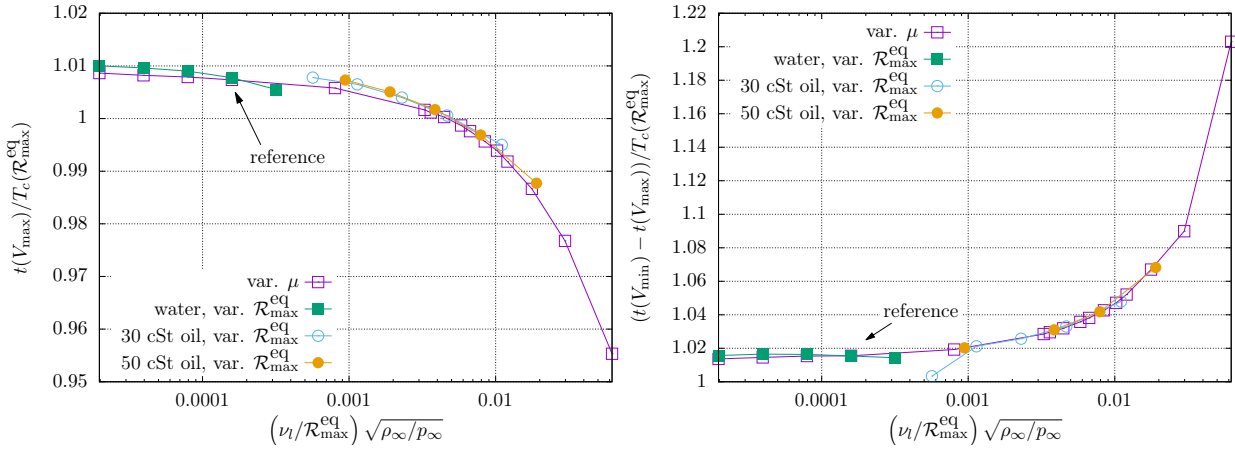


Fig. 7: Bubbles right at a flat solid boundary. Time from bubble inception to the maximum extension (left) and time from the maximum extension to the first collapse (right).

and  $113 \mu\text{s}$ ). The bubble shape during collapse resembles the shape of a bell.

The indentation sharpens and leads to an annular inflow, that arrives faster at the axis of symmetry, than the spherical cap comes down. As a result, the annular inflow impacts onto itself, momentarily generating a very high pressure (frame 6,  $t = 114.52 \mu\text{s}$ ). The self-impact leads to the emission of a shock wave and liquid is squeezed into the bubble in form of a very fast, thin jet (frames 7 and 8,  $t = 114.6 \mu\text{s}$  and  $114.8 \mu\text{s}$ ). The jet is also seen in Fig. 4 in the experimental photographs and the ray-traced numerical simulation in columns 7–9. Subsequently, the jet impacts onto the solid with a speed of the order of  $1000 \text{ m/s}$ , causing a large pressure load on the solid. Finally, the remaining torus bubble collapses, accompanied by the emission of a torus shock wave, see Fig. 5 (frame 9,  $t = 115.4 \mu\text{s}$ ).

## 5.2 Dynamics of bubbles expanding and collapsing right at a flat solid boundary – variation of bubble size and liquid viscosity

Depending on the viscosity of the liquid the bubbles in series 1 expand from the same initial data, see Sec. 4.1, to different maximum volumes, i.e. different  $\mathcal{R}_{\max}^{\text{eq}}$ . Figure 6 (left) shows the maximum equivalent radius  $\mathcal{R}_{\max}^{\text{eq}}$  as a function of  $\nu_l$ . As expected, the maximum radius decreases with increasing viscosity, as the portion of the bubble energy that is dissipated increases.

Figure 7 shows results from series 1–4. The left diagram shows the time from the initial conditions to the maximum extension,  $t(V_{\max})$ , normalized with the Rayleigh collapse time,

$$T_c := T_c(\mathcal{R}_{\max}^{\text{eq}}) = 0.915 \mathcal{R}_{\max}^{\text{eq}} \sqrt{\rho_{\infty}/p_{\infty}}, \quad (8)$$

of a bubble with radius  $\mathcal{R}_{\max}^{\text{eq}}$ . For low viscosity liquids this ratio is close to 1. With increasing viscosity or decreasing bubble size this quantity slightly decreases. The time from maximum extension to the first collapse, on the other hand, considerably decreases with increasing viscosity or decreasing bubble size, as shown in Fig. 7 (right). In total, expansion and collapse get more and more asymmetric with increasing viscosity or decreasing bubble size.

Figure 6 (right) shows the bubble shape at maximum extension for selected values of the inverse bubble Reynolds number including the reference bubble with  $1/\text{Re}_b = 1.6 \times 10^{-4}$ . The thickness of the viscous boundary layer during the expansion phase increases with increasing inverse bubble Reynolds number. As a consequence the distance of the outer rim of the bubble at maximum extension increases with increasing  $1/\text{Re}_b$ . Furthermore, with increasing inverse Reynolds number bubble expansion along the

solid wall is hindered and expansion in the direction orthogonal to the solid is increased. In total, the bubble shape changes from hemi-spherical with a slight “elevation” of the outer bubble rim for small inverse Reynolds numbers to a shape that resembles more an oblate spheroid for large inverse Reynolds numbers.

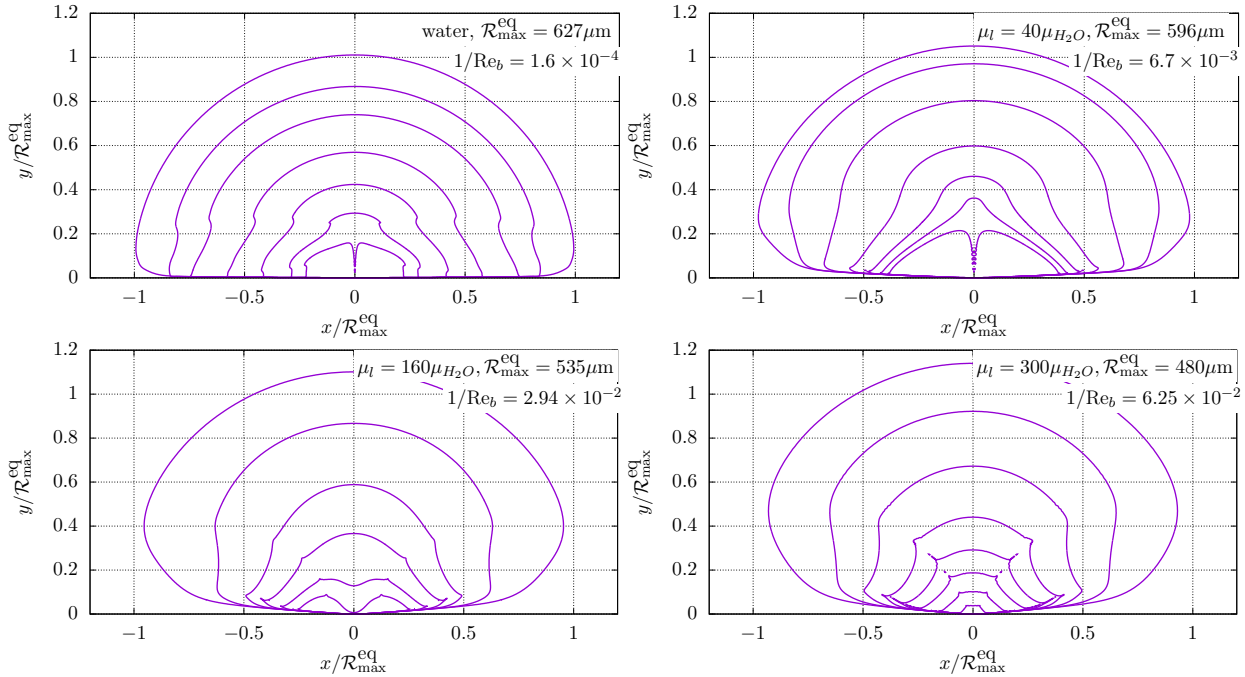


Fig. 8: Bubbles right at a flat solid boundary. Bubble shape during the collapse phase for four water-like (same density) liquids with viscosities  $\mu_l = \mu_{H_2O}$  (reference bubble),  $\mu_l = 40\mu_{H_2O}$ ,  $\mu_l = 160\mu_{H_2O}$ , and  $\mu_l = 300\mu_{H_2O}$ . The inverse bubble Reynolds numbers are  $1/Re_b = 1.59 \times 10^{-4}$ ,  $6.67 \times 10^{-3}$ ,  $2.94 \times 10^{-2}$ ,  $6.25 \times 10^{-2}$ . Time proceeds from outer to inner curves.

Figure 8 shows the bubble shapes during collapse for four liquids from series 1, including the reference bubble. In water with  $1/Re_b = 1.59 \times 10^{-4}$  the high curvature region at the outer bubble rim involutes and the bubble shape shows the indentation that has been described in Sec. 5.1. The indentation ultimately leads to the self impact of the annular inflow and the formation of the fast jet. For  $1/Re_b = 6.67 \times 10^{-3}$  (second frame) the higher curvature region at the outer bubble rim involutes as well. However, here the higher viscosity damps the relative motion and no annular inflow, faster than the surroundings, develops. The bubble surface stays smooth. The timing is such, that a spherical cap with higher curvature on top of the bubble is developing, which collapses faster than the bubble sides. A jet forms at the end of the collapse of the spherical cap by involution of the bubble wall. The speed of the jet for this value of  $1/Re_b$  amounts to approximately 500 m/s.

For even larger inverse Reynolds numbers  $1/Re_b = 2.94 \times 10^{-2}$  and  $6.25 \times 10^{-2}$  (Fig. 8 bottom row), there seem to be three regions during bubble collapse. A region close to the solid, where there is hardly any movement, a middle region around the “belly” of the bubble, which collapses faster and involutes, and a cap which seems to collapse in an approximately spherical manner. These three regions are indicated and separated by sharp edges in the bubble shape, which are more pronounced for the larger inverse Reynolds number. We note, that these sharp edges are not a numerical artefact, but are seen in the experiment as well, compare e.g. the shape of a collapsing bubble in PAO40 in Hupfeld et al. (2020). A broad jet with a speed of 110 m/s is formed by involution of the bubble wall for  $1/Re_b = 2.94 \times 10^{-2}$ . There is no jet formation for  $1/Re_b = 6.25 \times 10^{-2}$ .

Figure 9 shows the bubble shape and pressure field around jet formation for the bubbles with  $1/Re_b = 6.67 \times 10^{-3}$  and  $1/Re_b = 2.94 \times 10^{-2}$ . In Fig. 9 (A) the jet forms at the end of a fast collapsing spherical cap by involution of the bubble wall. A high pressure region forms due to the in-rushing liquid. The magnitude of pressure, however, is several orders of magnitude smaller than after the self-impact of annular inflow in Fig. 5 (frame 6,  $t = 114.52 \mu s$ ), above. The high pressure region connected to the broad jet in Fig. 9 (B) is one further order of magnitude smaller.

Figure 10 gives the jet speeds for all four series of simulations. For  $1/Re_b \gtrsim 3.3 \times 10^{-3}$  jets are formed by involution of the upper bubble wall, as shown in Fig. 8 and in Fig. 9 for  $1/Re_b = 6.67 \times 10^{-3}$  and  $2.94 \times 10^{-2}$ . Data points of all series of simulations collapse on a single line. For  $1/Re_b \lesssim 3.3 \times 10^{-3}$  fast jet formation is observed. Within a series of simulations, the jet speed seems to be roughly independent of  $1/Re_b$ , but differs between the series. We note, however, that the jet speed in the axially symmetric simulations numerically depends on the grid spacing, since jet formation arises from liquid self-impact at the axis, which is a nearly singular phenomenon. This is demonstrated in Appendix A.1 in Tab. A.1, where the jet speed for bubbles from series 2 with  $Re_b \approx 4 \times 10^{-5}$  and  $1/Re_b \approx 2 \times 10^{-5}$  are compared for two different grid resolutions. Nevertheless, we include these values of the jet speed here, since a trend in variation of the speed might be inferred from them.

Figure 10 (right) shows the equivalent radius of the bubble, which is a measure of bubble size, at the moment of jet formation,  $R_{jf}^{eq}$ . For fast jet formation and the jets forming after the collapse of a spherical cap, the moment of jet formation can be defined by a temporal pressure maximum at the axis. Data concerning the formation of a slow jet, as shown in Fig. 8 (second row, first frame) are not included in Fig. 10 (right), since this type of jet formation is not connected to a pressure maximum at the axis.

$R_{jf}^{eq}$  is maximum at  $1/Re_b \approx 0.01$  and decreases for smaller and larger  $1/Re_b$ . The transition from jet formation after the collapse

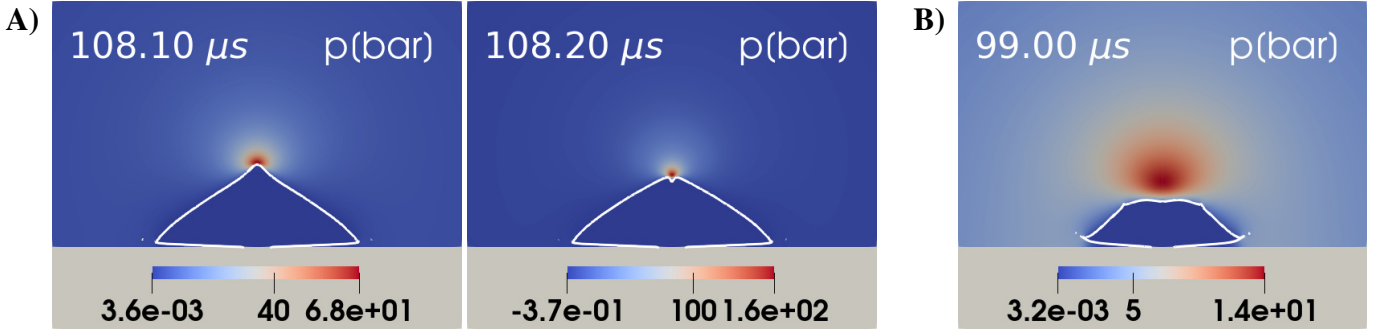


Fig. 9: Bubbles right at a flat solid boundary. Bubble shape and pressure field in bar around jet formation. **A)** Bubble with  $1/\text{Re}_b = 6.67 \times 10^{-3}$ , as in Fig. 8, top row, second frame and **B)** bubble with  $1/\text{Re}_b = 2.94 \times 10^{-2}$ , as in Fig. 8, bottom row, frame 1.

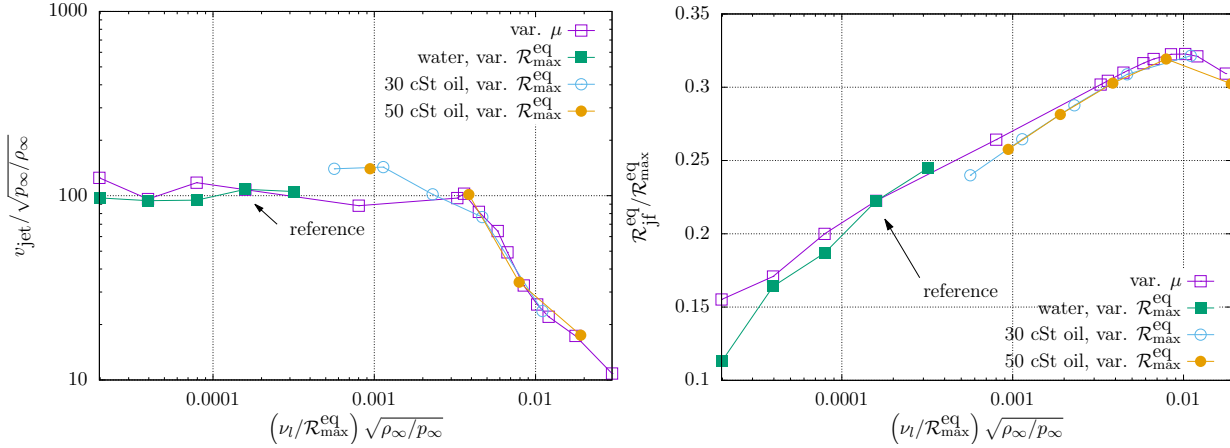


Fig. 10: Bubbles right at a flat solid boundary. Left: Normalized jet speed as a function of the inverse bubble Reynolds number. Right: Equivalent radius of the bubble at the moment of jet formation.

of a spherical cap to jet formation after self-impact of an annular inflow is smooth in the quantity  $\mathcal{R}_{jf}^{\text{eq}}$ . Decreasing  $1/\text{Re}_b$  further, fast jet formation happens later and later in the bubble evolution.

### 5.3 Mushroom bubbles

In the following the dynamics of a single bubble in water on top of a rigid cylinder is investigated both numerically and experimentally. Figure 11 shows the recording of a bubble at  $D^* = 0$ ,  $l_p \gg r_p$ ,  $r_p^* \approx 0.31$  with the photron camera. The radius of the cylinder top is  $r_p = 272.8 \mu\text{m}$ . Exposure time is  $1 \mu\text{s}$  and the recording frame rate is 21 kHz. Frame width is  $2012 \pm 104 \mu\text{m}$ . The bubble A has a half horizontal width of  $858 \mu\text{m} \pm 88 \mu\text{m}$  at  $95.24 \mu\text{s}$  and bubble B has a half horizontal width of  $851 \mu\text{m} \pm 88 \mu\text{m}$  at  $142.86 \mu\text{s}$ . When the bubble shape at that time instant is assumed as a sphere, subtracted by the volume of the rigid cylinder (taking also into account the slight frustrum deviation from the cylindrical shape), the equivalent radii of bubble A and B are:  $841 \mu\text{m} \pm 92 \mu\text{m}$  for bubble A and  $836 \mu\text{m} \pm 91 \mu\text{m}$  for bubble B. As shown in Koch et al. (2022), the ratio of  $R_{\text{max}}^{\text{eq}}$  to  $R_{\text{max}}^{\infty}$  is about 0.96 for  $D^* = 0$ . Applying this ratio to the corrected radii of bubble A and B, the value of  $r_p^*$  can be determined as  $0.31 \pm 0.03$  for both bubble A and B. Figure 12 shows the same bubbles A, B as in Fig. 11, but recorded with the Imacon camera. The time interval after the trigger pulse is denoted above each frame. The two series can be stacked together to show the dynamics that take place in and after frame 5 of Fig. 11A, B.

In order to classify the different parts of the shape of the bubble at different times, the terminology given in Figure 13 is applied. The dynamics of the bubbles in Figs. 11 and 12 can now be described in the following way: At first, the bubble expands to a radius about 3 times larger than the cylinder radius. Before minimum volume during collapse, the lower part seems to form a waist and the bottom of the bubble forms the *bottom stand foot*. When the neck tapers, the mushroom cap of the bubble becomes even more evident. During bubble volume minimum (during the end of sequence A and the beginning of sequence B in Fig. 12), the shape becomes cloudy by fragmentation into many small gas parts and subsequently the mushroom cap grows and detaches as a *projectile*.

In order to gain insight into why the mushroom shape of the bubble is formed and whether it is persistent to a wider range of the  $[D^*, r_p^*]$  parameter space, 89 simulations in axial symmetry have been performed, out of which 68 showed the mushroom shape (Koch et al. (2022)). 18 frames of one simulation with typical dynamics are shown in Fig. 14 with arrows indicating the main flow. The color indicates the magnitude of the velocity of the liquid in m/s. The characteristic values of the bubble are:  $R_{\text{max}}^{\infty} = 472.57 \mu\text{m}$ ,  $D^* = 0.063$ ,  $r_p^* = 0.423$ . The cylinder radius is  $200 \mu\text{m}$ . Frames 1–9 show the expansion and the beginning of the collapse, while frames 10–18 show the moment of jetting with a fast jet, the bubble minimum volume and rebound with the detaching of the projectile.

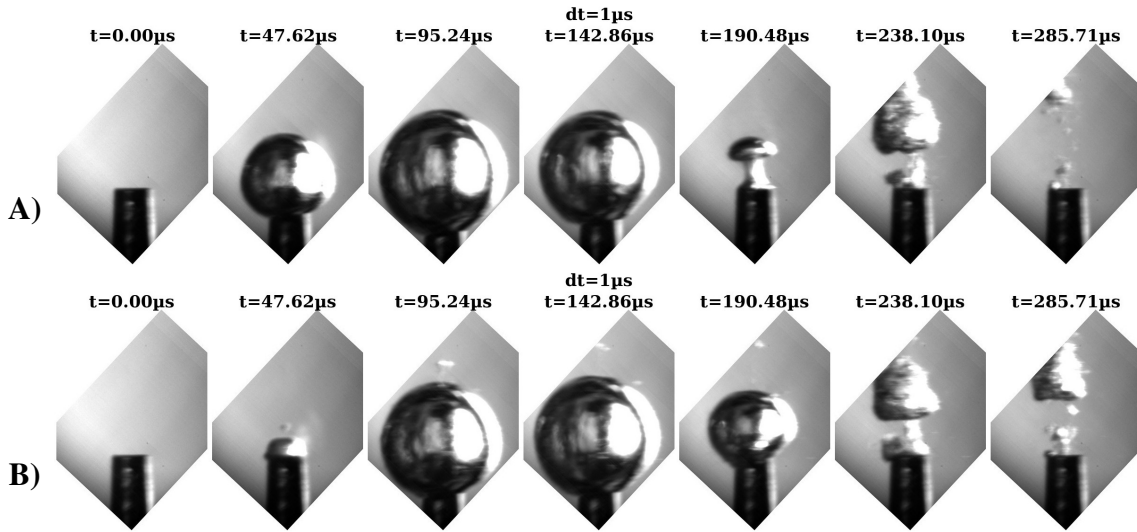


Fig. 11: Image sequence of two typical mushroom bubbles generated at  $D^* \approx 0$ ,  $l_p \gg r_p$ , recorded with the photron camera. The exposure time ( $dt$ ) of each frame is  $1 \mu\text{s}$  and the recording frame rate is  $21 \text{ kHz}$ .  $r_p$  is  $272.8 \mu\text{m}$ ,  $R_{\text{max}}^{\text{eq}}$  is about  $841 \mu\text{m}$  for bubble A and  $836 \mu\text{m}$  for bubble B, resulting in  $r_p^* \approx 0.31$  for both bubbles.

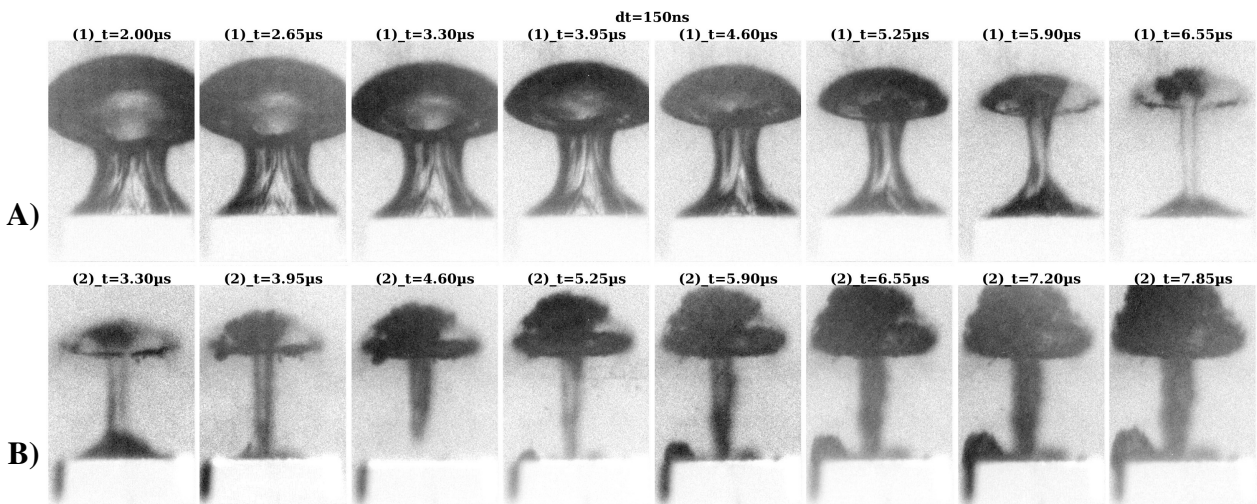


Fig. 12: Recording of the bubbles A, B of Fig. 11 with the Imacon camera. The time interval after the trigger pulse is denoted above each frame. The trigger time for bubble A is similar to the time of frame 5 in Fig. 11 and the trigger time for bubble B is between frame 5 and 6 in Fig. 11.

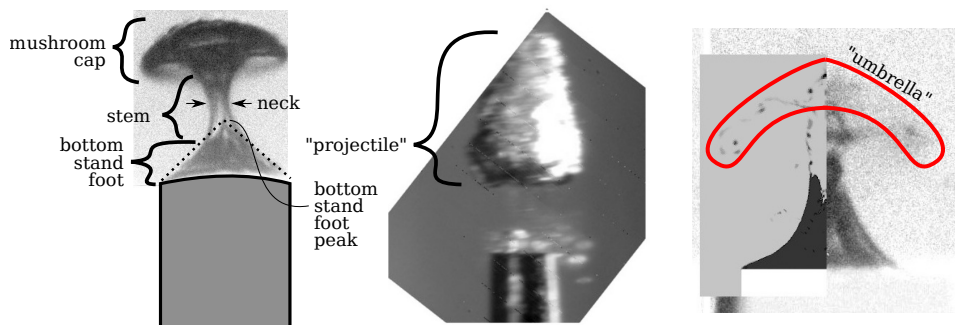


Fig. 13: Terminology for mushroom-shaped bubbles. Figure taken from Koch et al. (2022) under licence CC BY 4.0.

During the expansion phase, shown in the first 3 frames, the bubble interface crosses the cylinder rim, it swirls around it (frame 2), ejecting liquid droplets (in axial symmetry torus ring drops) into the bubble body. Once passed, these droplets hit the outer bubble interface, inducing surface waves there (dashed circles in frame 3). Due to the boundary layer around the cylinder, the bubble never touches the solid, but “swims” on the boundary layer.

When the bubble starts collapsing, the outer waist is lifted almost parallel to the cylinder. This flow produces the two annular inflows (in the 2D cut, an annular inflow in 3D) that form a) a neck and b) the extreme curvatures at the mushroom cap rim. As

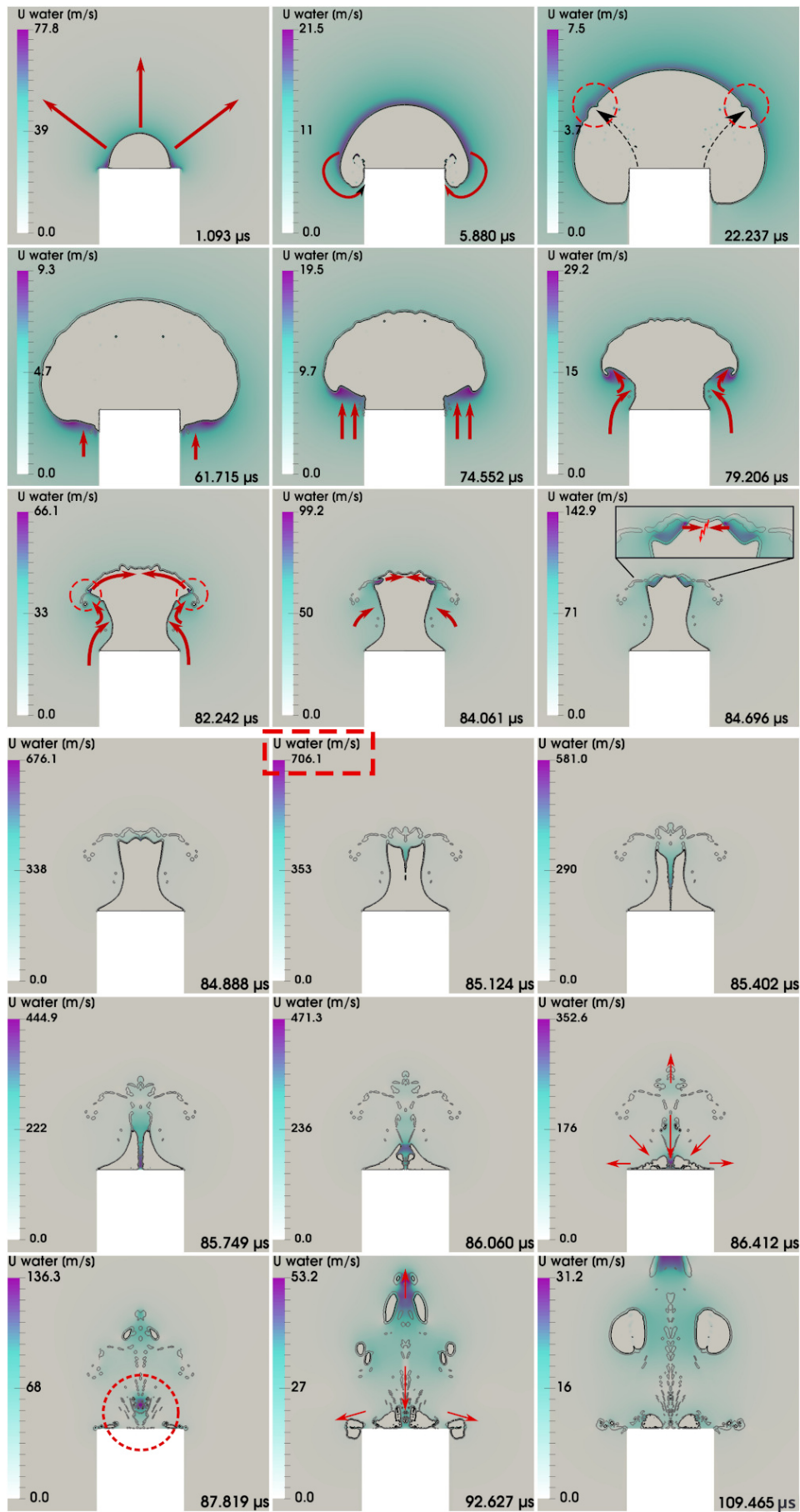


Fig. 14: General dynamics of the mushroom bubble. Figure taken from Koch et al. (2022) under licence CC BY 4.0.

denoted by the red arrows and circles in frame 7, Fig. 14, the flow that forms the mushroom neck has also a component upwards that tapers the cap to a thin gas film. The phenomenon of *flow focusing* comes into play Lauterborn (1982); Lechner et al. (2020),

flow focusing generating strongest acceleration where curvatures are highest. An annular jet is formed that runs along the top part of the shrinking mushroom cap, leaving trails of dim remnant gas that form a thin umbrella (see e.g. Fig. 13, right frame). Numerically, this results into a tearing of the interface, leaving areas where  $0.9 < \alpha < 1$ . In the end, this annular liquid jet impacts in the zenith of the umbrella, producing a *fast jet*. The fast jet actually is the reason, why the neck will not impact onto itself. It can be seen that the fast jet here reaches values of more than 700 m/s (see dashed rectangle on top of the velocity scale in frame 11). In some cases, it is more than 2000 m/s, as will be shown later. The liquid inflow from the top now, starting from frame 10 on, makes all sideways inflows at the neck negligible, changing the subsequent dynamics to a zipper-like collapse. The neck is tapered from inside rather than from outside flows. In the experiment, only the aforementioned “bottom stand foot” is observed here, because the outside bubble surface has too many wrinkles to see the jet inside. The minimum volume happens from top-down, thus the top gas fragments are already in the rebound phase, when the lower ones collapse and emit shock waves (not seen here – taking place in frame 16, as indicated by the dashed red circle in the frame). Therefore, the upper bubbles are “kicked” and squeezed upwards. Thereby, a layered structure of (torus) bubbles is observed.

Experimental insight into the moment of mushroom-bubble jetting can be gained with the Imacon camera. Figure 15 shows such a record of 8 frames at a time during annular jet impact at the zenith of the mushroom cap. The times denote the delay to the camera trigger. The recorded images are compared to a simulation via an overlay with the volume fraction field  $\alpha_l$  on the left side of each frame. Mind that the numerical simulation is represented by a cut through the bubble, therefore a ring in the experimental photograph appears as an off-axis gas dot in the simulation. The characteristic values for the bubble of the simulation are  $D^* = 0.057$  and  $r_p^* = 0.306$ . The frame width for the experiment is  $766 \mu\text{m} \pm 10 \mu\text{m}$ . The cylinder radius  $r_p$  in the experiment is  $272.8 \mu\text{m}$ , in the simulation  $r_p$  is  $200 \mu\text{m}$ . It is seen that the simulation and the experiment match very well, even the torus-shaped mushroom cap rim is reproduced by the simulation. It is also evident from the simulation that the stem/neck of the bubble is pierced by the fast jet, producing the top-down zipper-like collapse that is also seen in the experiment. For more comparisons, 3D simulations and experimental recordings, the reader again is referred to Koch et al. (2022).

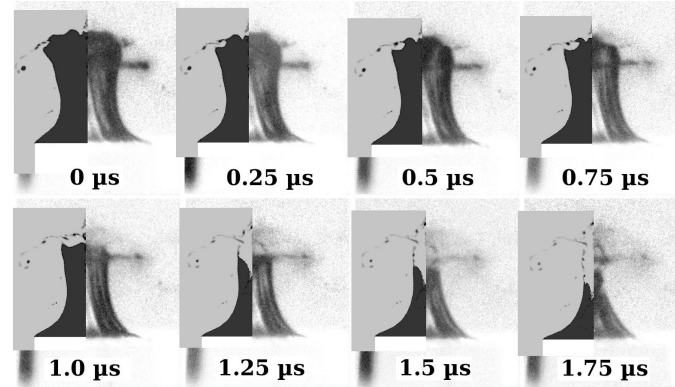


Fig. 15: Imacon camera frame sequence of a mushroom bubble at a time during ring jet impact at the top of the mushroom cap. Figure taken from Koch et al. (2022) under licence CC BY 4.0.

#### 5.4 Mushroom bubbles – numerical simulations – variation of $D^*$

The 89 simulations were evaluated and distinct quantities were extracted to be plotted into an interpolated heat map with isocurves within the  $[D^*, r_p^*]$  parameter space. The most prominent of the graphs from Koch et al. (2022) is shown in Figure 16. It shows the evaluation of the bubbles according to the jet velocity. It has to be noted, however, that due to the non-convergence of the velocity value, the graph is to be understood qualitatively. Each data point represents one simulation. The data points are plotted in their respective colors that represent their values. White data points denote cases, where either the bubble dynamics was different from the mushroom case, the annular jet impact happens later than the neck closure or a standard jet by involution of the bubble wall was observed.

The jet velocity was calculated by the distance of the spot of the annular jet impact to the top of the cylinder divided by the time the liquid needs to traverse this distance. This speed, however, did not converge yet for any mesh and time resolution (see explanation in Lechner et al. (2020); Koch et al. (2022)). Therefore, the values ranging from 189 m/s to 2164 m/s are given as tentative results. The corresponding water hammer pressures ( $\rho c v_{\text{jet}}$ ) would range from 0.3 GPa to 3 GPa. The heat map suggests that the faster jets are found for low values of  $r_p^*$  and higher values of  $D^*$ .

The dynamics of the cases along the  $D^*$ -axis for  $r_p^* = 0.251$  at 5 instants of time around the annular jet impact are shown in Fig. 17. As depicted in Fig. 16, only the two cases for  $D^* = 0.393$  and  $D^* = 0.550$  are considered as cases showing the described characteristics of the mushroom shape dynamics, though all cases shown in Fig. 17 more or less remind of a mushroom. However, the remaining cases show the *neck closing* (annular jet impact at the neck) before the annular jet impact in the zenith of the umbrella. That does not prevent a fast jet to happen, but the value for the fast-jet velocity becomes ambiguous since two to three fast jets can occur. From the neck closure, two jets may appear, one that is driven into the bottom stand foot, and also one upwards into the top of the bubble. Occasionally, like in the case of  $r_p^* = 0.251$ ;  $D^* = 0.236$ , the annular jet impact in the zenith of the umbrella still occurs, producing the third fast-jet. When only evaluating the velocity of the fast jet into the bottom stand foot, the maximum value of the set of simulations shown in Fig. 17 would be as high as 3245 m/s for  $D^* = 0.236$  and as low as 490 m/s for  $D^* = 0.629$ .

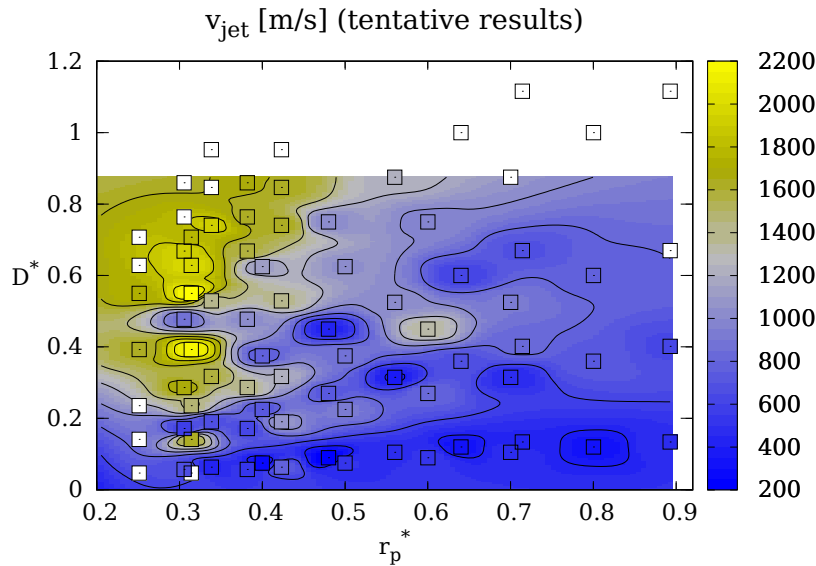


Fig. 16: Re-evaluation of the jet velocity (tentative results) of the 89 simulations performed for the parameter study in Koch et al. (2022). Each data point is one simulation. White points denote dynamics other than that of the mushroom bubbles.

From  $D^* = 0.550$  onward, the shape of the bubble reminds more of a trophy than of a mushroom.

## 6 Conclusion

The dynamics of bubbles expanding and collapsing right at a solid boundary has been investigated numerically for a range of bubble sizes and liquid viscosities. Furthermore, the dynamics of bubbles expanding and collapsing in water close to a different geometry, namely a rigid cylinder, have been studied numerically and experimentally with varying the geometry parameters: the normalized initial stand-off  $D^*$  and the normalized cylinder radius  $r_p^*$ .

For the bubbles right at the flat, solid boundary, we find the formation of a fast, thin jet after self-impact from an annular inflow for a wide range of combinations of bubble size and liquid viscosity. In terms of an inverse bubble Reynolds number,  $1/Re_b$ , as defined here, fast jet formation is found for  $1/Re_b \lesssim 0.0033$ . For smaller values of  $1/Re_b$  the formation of the fast jet happens later and later in the bubble evolution, whereas the average jet speed seems to be roughly independent of  $Re_b$ .

For  $1/Re_b \gtrsim 0.0033$  the jet formation mechanism changes and the jet forms by involution of the upper bubble wall. It has been demonstrated for  $1/Re_b = 6.67 \times 10^{-3}$  that the jet forms after a high curvature spherical cap has collapsed. For  $1/Re_b = 2.94 \times 10^{-3}$  a “slow”, broad jet is formed. The transition between these types of jet from involution of the bubble wall seems to be gradually. The jet speed continuously decreases with increasing  $1/Re_b$ . For  $1/Re_b = 6.25 \times 10^{-2}$  no jet is found, the bubble stays simply connected during the first collapse and beyond.

In the case of a laser-induced bubble on top of a long cylinder a dynamics very different from a bubble on an extended flat surface is found. After having embraced the cylinder top upon expansion, upon collapse it develops a mushroom shape with a head, a long stem and a footing. The simulation code has been validated again by comparison of an experimental with a numerical mushroom shape (Fig. 15). From the large set of parameters that has been studied in Koch et al. (2022) ( $0.047 \leq D^* \leq 2.009$  and  $0.251 \leq r_p^* \leq 0.893$ ) the jet velocity has been re-evaluated and the bubble shape transition from the mushroom shape to the trophy shape has been shown over  $D^*$  for  $r_p^* = 0.251$ .

The range of parameters shows that fast jets (studied numerically in Lechner et al. (2019); Pishchalnikov et al. (2019); Lechner et al. (2020) and experimentally in Koch (2020); Koch et al. (2021); Reuter and Ohl (2021) for bubbles close to a plane solid boundary) are not a singular phenomenon, but a robust phenomenon. It is expected to occur in many other configurations, too. The erosion potential of the fast jet appears high and is under actual investigation, see e.g. Reuter et al. (2022a). It may find applications in laser-induced ablation in liquids with pillars of various shapes as targets for laser synthesis and processing of colloids Zhang et al. (2017).

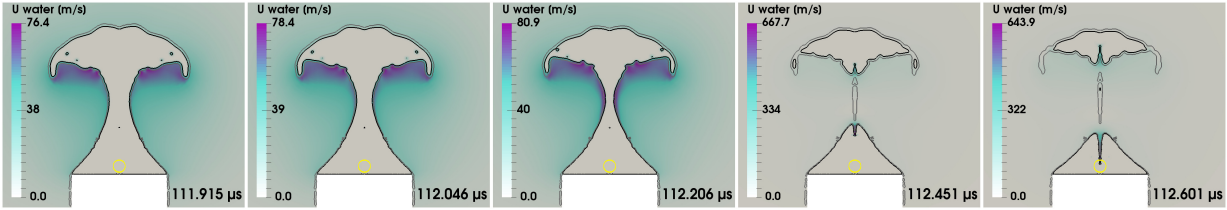
## Acknowledgments

The work was supported in part by the Austrian Science Fund (FWF) (Grant No. I 5349-N) and the German Science Foundation (DFG) under contracts ME 1645/8-1, ME 1645/8-3 and ME 1645/5-2.

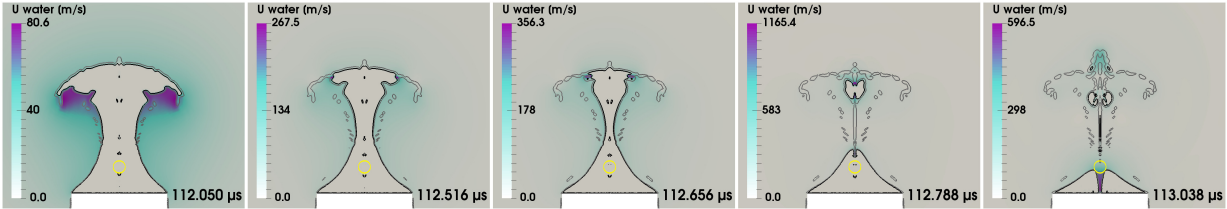
## Copyright information

Figures 1 (left), 2, 3 (left), 13, 14 and 15 are taken from Koch et al. (2022), Fig. 4 is taken from Koch et al. (2021). The figures are either modified or in original version as indicated in the captions. The sources of the figures are subject to the CC BY 4.0 license. Figure 3 (right) is adapted with permission from Lechner et al. (2020). Copyrighted by the American Physical Society.

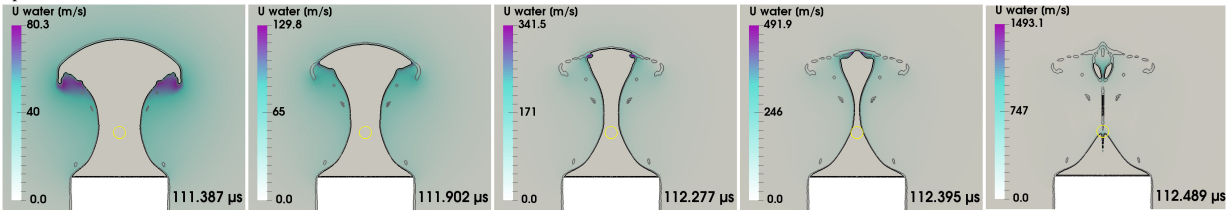
$r_p^* = 0.251 \quad D^* = 0.047$  (with neck closure):



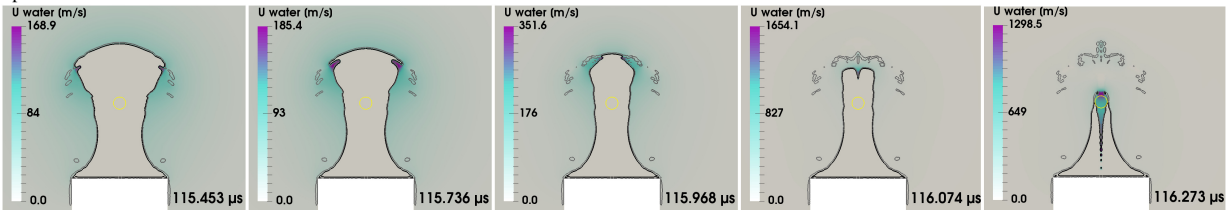
$r_p^* = 0.251 \quad D^* = 0.141$  (with neck closure):



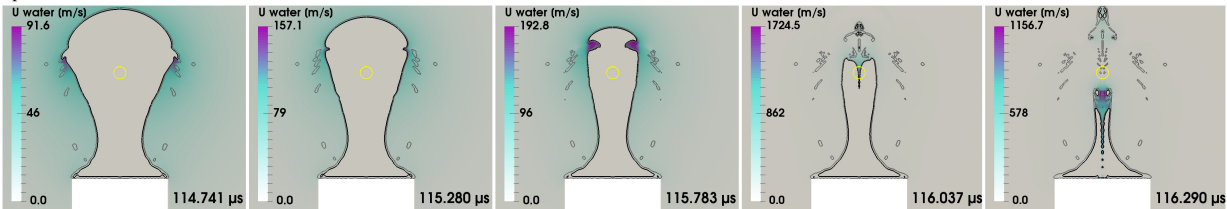
$r_p^* = 0.251 \quad D^* = 0.236$  (neck closure and fast jet almost at the same time):



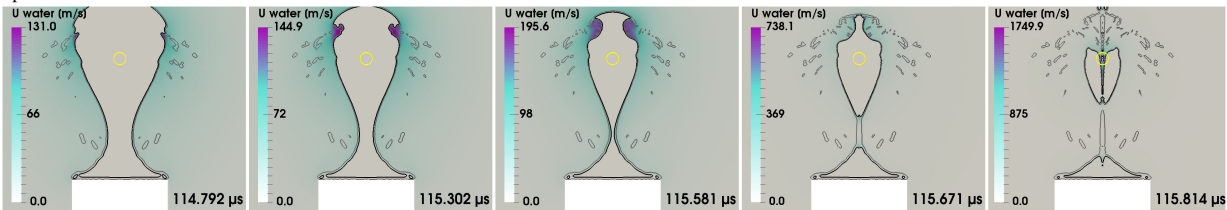
$r_p^* = 0.251 \quad D^* = 0.393$  (fast jet):



$r_p^* = 0.251 \quad D^* = 0.550$  (fast jet and beginning of trophy shape):



$r_p^* = 0.251 \quad D^* = 0.629$  (neck closure before the fast jet, trophy shape):



$r_p^* = 0.251 \quad D^* = 0.707$  (neck closure before the fast jet, trophy shape):

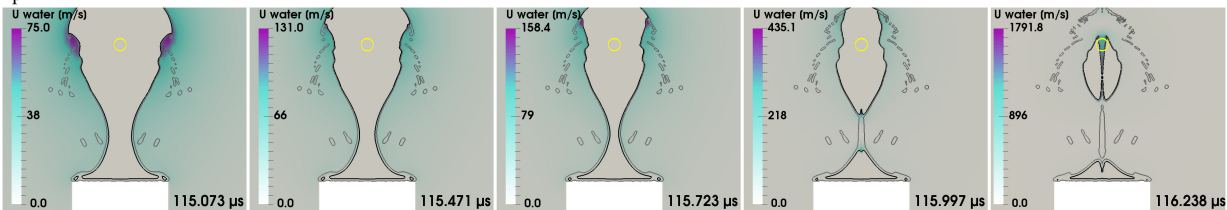


Fig. 17: Transition from mushroom shape to trophy shape for a bubble at  $r_p^* = 0.251$  for seven different values of  $D^*$ . The yellow circle denotes the initial bubble at  $t = 0$  which has a diameter of  $40 \mu\text{m}$ . The diameter of the cylinder is  $320 \mu\text{m}$ .

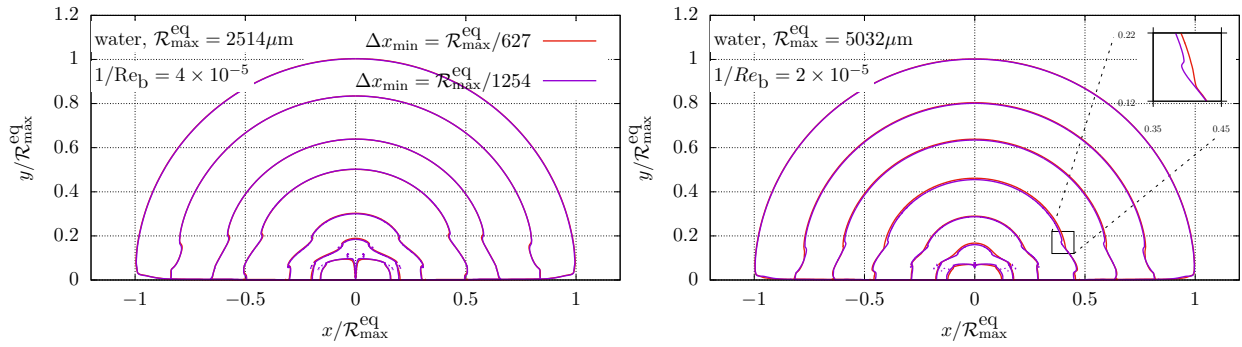


Fig. A.1: Collapse of a bubble in water. Shown are the bubble shapes of two simulations with different grid resolution,  $\Delta x_{\min} = \mathcal{R}_{\max}^{\text{eq}}/627$  and  $\Delta x_{\min} = \mathcal{R}_{\max}^{\text{eq}}/1254$ . Left:  $\mathcal{R}_{\max}^{\text{eq}} = 2514 \mu\text{m}$ , time instants shown are  $t = 230.5, 370, 420, 440, 456, 460, 461 \mu\text{s}$  (coarser grid) and  $t = 230, 369, 419, 439, 455.2, 459.2, 460.1 \mu\text{s}$  (finer grid). Right:  $\mathcal{R}_{\max}^{\text{eq}} = 5032 \mu\text{m}$ , time instants shown are  $t = 460, 760, 840, 889, 914, 922, 924 \mu\text{s}$  (coarser grid) and  $t = 460, 760, 840, 889, 913, 921, 922.7 \mu\text{s}$  (finer grid). The last time step is taken shortly after the formation of the fast jet. The inset shows the kink in the bubble shape at  $t = 889 \mu\text{s}$ .

$\Delta x_{\min}$ [ $\mu\text{m}$ ]	$\mathcal{R}_{\max}^{\text{eq}}$ [ $\mu\text{m}$ ]	$t(V_{\max})$ [ $\mu\text{s}$ ]	$t(V_{\min})$ [ $\mu\text{s}$ ]	$\mathcal{R}_{\text{jf}}^{\text{eq}}$ [ $\mu\text{m}$ ]	$v_j$ [m/s]
4	2514	231	462.58	413	947
2	2511	230	461.36	389	1926
8	5032	462	925.76	568	980
4	5025	461	924.27	597	1487

Tab. A.1: Dependence of bubble dynamics on the grid size for bubbles in water

## Appendix

### A.1 Bubbles right at a flat solid boundary – grid independence study

Bubbles with  $\mathcal{R}_{\max}^{\text{eq}} \approx 627 \mu\text{m}$  oscillating right at a flat solid boundary in water have been investigated in Lechner et al. (2020). There, it has been demonstrated that a grid with  $\Delta x_{\min} = 1 \mu\text{m} \approx \mathcal{R}_{\max}^{\text{eq}}/627$  is sufficient to resolve the dynamics of the bubble including fast jet formation. However, since the self-impact of the annular jet at the axis of symmetry is a nearly singular process in axial symmetry, convergence of the jet speed could not be achieved, no matter how fine the grid in the inner region was chosen. The simulations in Sec. 5.2, series 2 (the liquid is water and the maximum bubble size is varied) are performed on grids with a minimum grid spacing of  $\Delta x_{\min} = \mathcal{R}_{\max}^{\text{eq}}/627$ , i.e. the grid is scaled with the maximum bubble radius. Since the liquid gap between the outer bubble rim and the solid decreases in relation to  $\mathcal{R}_{\max}^{\text{eq}}$  when  $1/\text{Re}_b$  is decreased (compare Fig. 6 (right)), the question arises, whether this gap and the high curvature of the bubble wall is sufficiently resolved. Fig. A.1 shows the influence of the grid spacing on the collapse phase of bubbles with  $\mathcal{R}_{\max}^{\text{eq}} = 2514 \mu\text{m}$  and  $\mathcal{R}_{\max}^{\text{eq}} = 5032 \mu\text{m}$ . The grid with a minimum grid spacing of  $\Delta x_{\min} = \mathcal{R}_{\max}^{\text{eq}}/627$  is used for the simulations in Sec. 5.2. Doubling the resolution to  $\Delta x_{\min} = \mathcal{R}_{\max}^{\text{eq}}/1254$  yields bubble shapes that agree very well both in space and time. For the smaller bubble, displayed in Fig. A.1 (left), the sharp kinks that form during the collapse phase are well resolved with both resolutions. For the larger bubble with  $\mathcal{R}_{\max}^{\text{eq}} = 5032 \mu\text{m}$  shown in Fig. A.1 (right), the kink that develops at a distance  $y \lesssim 0.2\mathcal{R}_{\max}^{\text{eq}}$  from the solid only is resolved on the finer grid, whereas it is smoothed on the coarser grid. This smoothing leads to a weaker self-impact at the axis (not shown). Key quantities describing the dynamics of the bubbles are given in Tab. A.1 for the two bubbles and two resolutions. The collapse time hardly changes when doubling the resolution. The equivalent radius of the bubble at the moment of jet formation  $\mathcal{R}_{\text{jf}}^{\text{eq}}$  changes by a few percent. This amount is considered as small enough as not to change the conclusions that can be drawn from Fig. 10 (right). A grid with  $\Delta x_{\min} = \mathcal{R}_{\max}^{\text{eq}}/627$  therefore is considered as sufficient for the present study.

The speed of the fast jet varies considerably when doubling the resolution. This agrees with previous findings and has been discussed in (Lechner et al., 2020, Appendix B). In axial symmetry, convergence with grid resolution cannot be expected for the jet speed. Concerning the fast jet regimes in Fig. 10 (left) and also in Fig. 16 the values only are valid for a certain grid resolution.

## References

- Elijah D. Andrews, David Fernández Rivas, and Ivo R. Peters. Cavity collapse near slot geometries. *J. Fluid Mech.*, 901:A29–1–22, Sep 2020. doi: [10.1017/jfm.2020.552](https://doi.org/10.1017/jfm.2020.552).
- T. B. Benjamin and A. T. Ellis. The collapse of cavitation bubbles and the pressures thereby produced against solid boundaries. *Philos. Trans. R. Soc. London, Ser. A*, 260:221–240, 1966. doi: [10.1098/rsta.1966.0046](https://doi.org/10.1098/rsta.1966.0046).
- Emil-Alexandru Brujan, Kester Nahen, Peter Schmidt, and Alfred Vogel. Dynamics of laser-induced cavitation bubbles near elastic boundaries: influence of the elastic modulus. *J. Fluid Mech.*, 433:283–314, 2001. doi: [10.1017/S0022112000003335](https://doi.org/10.1017/S0022112000003335).
- Emil-Alexandru Brujan, Tatsuya Noda, Atsushi Ishigami, Toshiyuki Ogasawara, and Hiroyuki Takahira. Dynamics of laser-induced cavitation bubbles near two perpendicular rigid walls. *J. Fluid Mech.*, 841:28–49, Feb 2018. doi: [10.1017/jfm.2018.82](https://doi.org/10.1017/jfm.2018.82).

- CC BY 4.0. Creative Commons Attribution License 4.0. URL <https://creativecommons.org/licenses/by/4.0/>.
- Silvestre Roberto Gonzalez Avila, Chaolong Song, and Claus-Dieter Ohl. Fast transient microjets induced by hemispherical cavitation bubbles. *J. Fluid Mech.*, 767:31–51, 2015. doi: [10.1017/jfm.2015.33](https://doi.org/10.1017/jfm.2015.33).
- Silvestre Roberto Gonzalez-Avila, Anne Charlotte van Blokland, Qingyun Zheng, and Claus-Dieter Ohl. Jetting and shear stress enhancement from cavitation bubbles collapsing in a narrow gap. *J. Fluid Mech.*, 884:A23–1 – A32–23, 2020. doi: [10.1017/jfm.2019.938](https://doi.org/10.1017/jfm.2019.938).
- Bernhard Gschaider, Håkan Nilsson, Henrik Rusche, Hrvoje Jasak, Martin Beaudoin, and Vanja Skuric. The foam-extend project, 2017. URL <https://sourceforge.net/projects/foam-solidboundaryextend/>.
- C.-T. Hsiao, J.-K. Choi, S. Singh, G. L. Chahine, T. A. Hay, Yu. A. Ilinskii, E. A. Zabolotskaya, M. F. Hamilton, G. Sankin, F. Yuan, and et al. Modelling single- and tandem-bubble dynamics between two parallel plates for biomedical applications. *J. Fluid Mech.*, 716:137–170, 2013. doi: [10.1017/jfm.2012.526](https://doi.org/10.1017/jfm.2012.526).
- Tim Hupfeld, Gaëtan Laurens, Samy Merabia, Stephan Barcikowski, Bilal Gökce, and David Amans. Dynamics of laser-induced cavitation bubbles at a solid–liquid interface in high viscosity and high capillary number regimes. *J. Appl. Phys.*, 127(4):044306, Jan 2020. doi: [10.1063/1.5116111](https://doi.org/10.1063/1.5116111).
- Ebrahim Kadivar, Ould el Moctar, Romuald Skoda, and Udo Löschner. Experimental study of the control of cavitation-induced erosion created by collapse of single bubbles using a micro structured riblet. *Wear*, 486-487:204087, 2021a. ISSN 0043-1648. doi: [10.1016/j.wear.2021.204087](https://doi.org/10.1016/j.wear.2021.204087).
- Ebrahim Kadivar, Thanh-Hoang Phan, Warn-Gyu Park, and Ould el Moctar. Dynamics of a single cavitation bubble near a cylindrical rod. *Phys. Fluids*, 33(11):113315–1–19, Nov 2021b. doi: [10.1063/5.0070847](https://doi.org/10.1063/5.0070847).
- Badarinath Karri, Kiran S. Pillai, Evert Klaseboer, Siew-Wan Ohl, and Boo Cheong Khoo. Collapsing bubble induced pumping in a viscous fluid. *Sensors and Actuators A: Physical*, 169(1):151–163, 2011. ISSN 0924-4247. doi: [10.1016/j.sna.2011.04.015](https://doi.org/10.1016/j.sna.2011.04.015).
- Markus Kauer, Valentina Belova-Magri, Carlos Cairós, Gerd Linka, and Robert Mettin. High-speed imaging of ultrasound driven cavitation bubbles in blind and through holes. *Ultrason. Sonochem.*, 48:39–50, 2018. doi: [10.1016/j.ultsonch.2018.04.015](https://doi.org/10.1016/j.ultsonch.2018.04.015).
- Donghyun Kim and Daegyoum Kim. Underwater bubble collapse on a ridge-patterned structure. *Phys. Fluids*, 32(5):053312, May 2020. doi: [10.1063/5.0006372](https://doi.org/10.1063/5.0006372).
- Max Koch. *Laser cavitation bubbles at objects: Merging numerical and experimental methods*. PhD thesis, Georg-August-Universität Göttingen, Third Physical Institute, 2020. doi: [10.53846/goediss-solidboundary8326](https://doi.org/10.53846/goediss-solidboundary8326).
- Max Koch, Christiane Lechner, Fabian Reuter, Karsten Köhler, Robert Mettin, and Werner Lauterborn. Numerical modeling of laser generated cavitation bubbles with the finite volume and volume of fluid method, using OpenFOAM. *Comput. Fluids*, 126: 71–90, 2016. doi: [10.1016/j.compfluid.2015.11.008](https://doi.org/10.1016/j.compfluid.2015.11.008).
- Max Koch, Juan M. Rosselló, Christiane Lechner, Werner Lauterborn, Julian Eisener, and Robert Mettin. Theory-assisted optical ray tracing to extract cavitation-bubble shapes from experiment. *Exp. Fluids*, 62(3):60, Mar 2021. doi: [10.1007/s00348-020-03075-6](https://doi.org/10.1007/s00348-020-03075-6).
- Max Koch, Juan Manuel Rosselló, Christiane Lechner, Werner Lauterborn, and Robert Mettin. Dynamics of a laser-induced bubble above the flat top of a solid cylinder—mushroom-shaped bubbles and the fast jet. *Fluids*, 7(1):2, 2022. doi: [10.3390/fluids7010002](https://doi.org/10.3390/fluids7010002).
- W. Lauterborn. Bubble generation by giant laser pulses and resonance curves of gas bubbles in water. In L. I. Sedov and G. Yu. Stepanov, editors, *Non-steady flow of water at high speeds. Proceedings of the IUTAM Symposium held in Leningrad*, pages 267–275, 1971.
- W. Lauterborn. Cavitation bubble dynamics — new tools for an intricate problem. *Appl. Sci. Res.*, 38(1):165–178, 1982. doi: [10.1007/BF00385946](https://doi.org/10.1007/BF00385946).
- Werner Lauterborn, Christiane Lechner, Max Koch, and Robert Mettin. Bubble models and real bubbles: Rayleigh and energy-deposit cases in a Tait-compressible liquid. *IMA J. Appl. Math.*, 83:556–589, 2018. doi: [10.1093/imamat/hxy015](https://doi.org/10.1093/imamat/hxy015).
- Christiane Lechner, Werner Lauterborn, Max Koch, and Robert Mettin. Fast, thin jets from bubbles expanding and collapsing in extreme vicinity to a solid boundary: A numerical study. *Phys. Rev. Fluids*, 4:021601, Feb 2019. doi: [10.1103/PhysRevFluids.4.021601](https://doi.org/10.1103/PhysRevFluids.4.021601).
- Christiane Lechner, Werner Lauterborn, Max Koch, and Robert Mettin. Jet formation from bubbles near a solid boundary in a compressible liquid: Numerical study of distance dependence. *Phys. Rev. Fluids*, 5(9):093604, Sep 2020. doi: [10.1103/physrevfluids.5.093604](https://doi.org/10.1103/physrevfluids.5.093604).
- Shuai Li, A-Man Zhang, Rui Han, and Qingwei Ma. 3D full coupling model for strong interaction between a pulsating bubble and a movable sphere. *J. Comput. Phys.*, 392:713–731, Sep 2019. doi: [10.1016/j.jcp.2019.05.001](https://doi.org/10.1016/j.jcp.2019.05.001).
- H. F. Okorn-Schmidt, F. Holsteyns, A. Lippert, D. Mui, M. Kawaguchi, C. Lechner, P. E. Frommhold, T. Nowak, F. Reuter, M. Banchs Piqué, C. Cairós, and R. Mettin. Particle cleaning technologies to meet advanced semiconductor device process requirements. *ECS Journal of Solid State Science and Technology*, 3(1):N3069–N3080, 2014. doi: [10.1149/2.011401jss](https://doi.org/10.1149/2.011401jss).
- Daniel Palanker, Alexander Vankov, Jason Miller, Menahem Friedman, and Moshe Strauss. Prevention of tissue damage by water jet during cavitation. *J. Appl. Phys.*, 94(4):2654–2661, Aug 2003. doi: [10.1063/1.1593803](https://doi.org/10.1063/1.1593803).
- A. Philipp and W. Lauterborn. Cavitation erosion by single laser-produced bubbles. *J. Fluid Mech.*, 361:75–116, 1998. doi: [10.1017/S0022112098008738](https://doi.org/10.1017/S0022112098008738).

- Yuri A. Pishchalnikov, William M. Behnke-Parks, Kevin Schmidmayer, Kazuki Maeda, Tim Colonius, Thomas W. Kenny, and Daniel J. Laser. High-speed video microscopy and numerical modeling of bubble dynamics near a surface of urinary stone. *J. Acoust. Soc. Am.*, 146:516 – 531, 2019. doi: [10.1121/1.5116693](https://doi.org/10.1121/1.5116693).
- Edmund Wenjie Quah, Badarinath Karri, Siew-Wan Ohl, Evert Klaseboer, and Boo Cheong Khoo. Expansion and collapse of an initially off-centered bubble within a narrow gap and the effect of a free surface. *International Journal of Multiphase Flow*, 99: 62–72, 2018. ISSN 0301-9322. doi: [10.1016/j.ijmultiphaseflow.2017.09.013](https://doi.org/10.1016/j.ijmultiphaseflow.2017.09.013).
- Fabian Reuter and Robert Mettin. Mechanisms of single bubble cleaning. *Ultrason. Sonochem.*, 29:550–562, 2016. doi: [10.1016/j.ultsonch.2015.06.017](https://doi.org/10.1016/j.ultsonch.2015.06.017).
- Fabian Reuter and Claus-Dieter Ohl. Supersonic needle-jet generation with single cavitation bubbles. *Appl. Phys. Letters*, 118(13): 134103, Mar 2021. doi: [10.1063/5.0045705](https://doi.org/10.1063/5.0045705).
- Fabian Reuter, Carsten Deiter, and Claus-Dieter Ohl. Cavitation erosion by shockwave self-focusing of a single bubble. *Ultrason. Sonochem.*, page 106131, Nov 2022a. doi: [10.1016/j.ultsonch.2022.106131](https://doi.org/10.1016/j.ultsonch.2022.106131).
- Fabian Reuter, Qingyun Zeng, and Claus-Dieter Ohl. The Rayleigh prolongation factor at small bubble to wall stand-off distances. *J. Fluid Mech.*, 944, Jun 2022b. doi: [10.1017/jfm.2022.475](https://doi.org/10.1017/jfm.2022.475).
- Mandeep Saini, Erwan Tanne, Michel Arrigoni, Stephane Zaleski, and Daniel Fuster. On the dynamics of a collapsing bubble in contact with a rigid wall. *J. Fluid Mech.*, 948:A45–1–A45–19, Sep 2022. doi: [10.1017/jfm.2022.705](https://doi.org/10.1017/jfm.2022.705).
- Matej Senegačnik, Kohei Kunimoto, Satoshi Yamaguchi, Koki Kimura, Tetsuo Sakka, and Peter Gregorčič. Dynamics of laser-induced cavitation bubble during expansion over sharp-edge geometry submerged in liquid – an inside view by diffuse illumination. *Ultrason. Sonochem.*, 73:105460, May 2021. doi: [10.1016/j.ultsonch.2021.105460](https://doi.org/10.1016/j.ultsonch.2021.105460).
- Outi Supponen, Danaïl Obreschkow, Marc Tinguely, Philippe Kobel, Nicolas Dorsaz, and Mohamed Farhat. Scaling laws for jets of single cavitation bubbles. *J. Fluid Mech.*, 802:263–293, 2016. doi: [10.1017/jfm.2016.463](https://doi.org/10.1017/jfm.2016.463).
- Y. Tomita, P. B. Robinson, and R. P. Tong. Growth and collapse of cavitation bubbles near a curved rigid boundary. *J. Fluid Mech.*, 466:259–283, 2002. doi: [10.1017/S0022112001209](https://doi.org/10.1017/S0022112001209).
- Theresa Trummler, Spencer H. Bryngelson, Kevin Schmidmayer, Steffen J. Schmidt, Tim Colonius, and Nikolaus A. Adams. Near-surface dynamics of a gas bubble collapsing above a crevice. *J. Fluid Mech.*, 899:A16–1–21, Jul 2020. doi: [10.1017/jfm.2020.432](https://doi.org/10.1017/jfm.2020.432).
- G. Tryggvason, B. Brunner, A. Esmaeeli, D. Juric, N. Al-Rawahi, W. Tauber, J. Han, S. Nas, and Y.-J. Jan. A front-tracking method for the computations of multiphase flow. *J. Comput. Phys.*, 169:708–759, 2001. doi: [10.1006/jcph.2001.6726](https://doi.org/10.1006/jcph.2001.6726).
- Qianxi Wang, Mehdi Mahmud, Jie Cui, Warren R. Smith, and A. D. Walmsley. Numerical investigation of bubble dynamics at a corner. *Phys. Fluids*, 32(5):053306, May 2020. doi: [10.1063/1.5140740](https://doi.org/10.1063/1.5140740).
- H. G. Weller, G. Tabor, H. Jasak, and C. Fureby. A tensorial approach to computational continuum mechanics using object-oriented techniques. *Comput. Phys.*, 12(6):620–631, 1998. doi: [10.1063/1.168744](https://doi.org/10.1063/1.168744).
- Tatsuya Yamashita and Keita Ando. Low-intensity ultrasound induced cavitation and streaming in oxygen-supersaturated water: Role of cavitation bubbles as physical cleaning agents. *Ultrasonics Sonochemistry*, 52:268–279, 2019. doi: [10.1016/j.ultsonch.2018.11.025](https://doi.org/10.1016/j.ultsonch.2018.11.025).
- Jure Zevnik and Matevž Dular. Cavitation bubble interaction with a rigid spherical particle on a microscale. *Ultrasonics Sonochemistry*, 69:105252, 2020. doi: [10.1016/j.ultsonch.2020.105252](https://doi.org/10.1016/j.ultsonch.2020.105252).
- Dongshi Zhang, Bilal Gökce, and Stephan Barcikowski. Laser synthesis and processing of colloids: Fundamentals and applications. *Chem. Rev.*, 117(5):3990–4103, Feb 2017. doi: [10.1021/acs.chemrev.6b00468](https://doi.org/10.1021/acs.chemrev.6b00468).
- Yuning Zhang, Xu Qiu, Xiangqing Zhang, Ningning Tang, and Yuning Zhang. Collapsing dynamics of a laser-induced cavitation bubble near the edge of a rigid wall. *Ultrason. Sonochem.*, 67:105157, Oct 2020. doi: [10.1016/j.ultsonch.2020.105157](https://doi.org/10.1016/j.ultsonch.2020.105157).